Evolution of dust porosity through coagulation and shattering in the interstellar medium

Hiroyuki Hirashita,[1]⋆ Vladimir B. Il'in,[2,3,4] Laurent Pagani[5] and Charlène Lefèvre[6,5]

[1]*Institute of Astronomy and Astrophysics, Academia Sinica, Astronomy-Mathematics Building, No. 1, Section 4,*
Roosevelt Road, Taipei 10617, Taiwan
[2]*St Petersburg State University, Universitetskij Pr. 28, St Petersburg 198504, Russia*
[3]*Pulkovo Observatory, Pulkovskoe Sh. 65/1, St Petersburg 196140, Russia*
[4]*St Petersburg University of Aerospace Instrumentation, Bol. Morskaya 67, St Petersburg 190000, Russia*
[5]*LERMA & UMR8112 du CNRS, Observatoire de Paris, PSL University, Sorbonne Universités, CNRS, F-75014 Paris, France*
[6]*Institut de Radioastronomie Millimétrique (IRAM), 300 rue de la Piscine, 38400 Saint-Martin d'Hères, France*

ABSTRACT

The properties of interstellar grains, such as grain size distribution and grain porosity, are affected by interstellar processing, in particular, coagulation and shattering, which take place in the dense and diffuse interstellar medium (ISM), respectively. In this paper, we formulate and calculate the evolution of grain size distribution and grain porosity through shattering and coagulation. For coagulation, we treat the grain evolution depending on the collision energy. Shattering is treated as a mechanism of forming small compact fragments. The balance between these processes are determined by the dense-gas mass fraction η_{dense}, which determines the time fraction of coagulation relative to shattering. We find that the interplay between shattering supplying small grains and coagulation forming porous grains from shattered grains is fundamentally important in creating and maintaining porosity. The porosity rises to 0.7–0.9 (or the filling factor 0.3–0.1) around grain radii $a \sim 0.1$ μm. We also find that, in the case of $\eta_{\mathrm{dense}} = 0.1$ (very efficient shattering with weak coagulation) porosity significantly enhances coagulation, creating fluffy submicron grains with filling factors lower than 0.1. The porosity enhances the extinction by 10–20 per cent at all wavelengths for amorphous carbon and at ultraviolet wavelengths for silicate. The extinction curve shape of silicate becomes steeper if we take porosity into account. We conclude that the interplay between shattering and coagulation is essential in creating porous grains in the interstellar medium and that the resulting porosity can impact the grain size distributions and extinction curves.

Key words: methods: numerical – dust, extinction – ISM: evolution – galaxies: ISM – scattering – ultraviolet: ISM

1 INTRODUCTION

Dust grains are important for various processes in the interstellar medium (ISM) and in galaxies. Not only the total dust abundance but also the distribution function of grain radius, referred to as the grain size distribution, is important, since under a given dust abundance, the total surface area and the cross-section of light absorption and scattering (extinction) are governed by the grain size distribution. Since H$_2$ forms on dust surfaces (e.g. Gould & Salpeter 1963; Cazaux & Tielens 2004), the total surface area of dust grains affects the H$_2$ formation rate, which could influence the galaxy evolution (e.g. Yamasawa et al. 2011; Chen et al. 2018). The extinction cross-section as a function of wavelength, referred to as the extinction curve, gives us a clue to the grain size distribution (e.g. Mathis et al. 1977, hereafter MRN). The extinction curve is strongly modified by dust evolution (e.g. Asano et al. 2014). The evolution of grain size distribution also affects the spectral energy distributions (SEDs) of galaxies (e.g. Désert et al. 1990; Takeuchi et al. 2005). Thus, the evolution of grain size distribution is of fundamental importance in

understanding the chemical and radiative processes in the ISM and in galaxies.

The evolution of dust in the ISM or in galaxies is governed by various processes (e.g. Lisenfeld & Ferrara 1998; Draine 2009). The major processes for the dust enrichment are stellar dust production and dust growth in the ISM (e.g. Dwek 1998). Dust destruction in supernova shocks (e.g. McKee 1989) is considered to dominate the decrease of dust in the ISM. In the Milky Way environment, since the metallicity is high enough, dust growth by the accretion of gas-phase metals can be efficient enough to balance the dust destruction (e.g. Draine 1990; Dwek 1998; Hirashita 1999; Inoue 2011; Mattsson et al. 2014). This accretion process, which is also verified in some experiments (Rouillé et al. 2014, 2020), occurs in the dense ISM. The grain size distribution, on the other hand, is strongly modified by coagulation in the dense ISM and shattering in the diffuse ISM (e.g. O'Donnell & Mathis 1997; Hirashita & Yan 2009). Although some of the above processes occur either in a certain phase of the ISM, all dust processes eventually affect the mean properties of interstellar dust through a quick ($\sim 10^7$ yr) exchange between various ISM phases (e.g. McKee 1989). The abundance ratio between large and small grains is roughly determined by the balance between coagulation and shattering (Hirashita & Aoyama 2019).

⋆ E-mail: hirashita@asiaa.sinica.edu.tw

If coagulation and shattering govern the functional shape of grain size distribution as suggested by previous studies, these processes could put a clear imprint on the grain properties. In particular, coagulation could form inhomogeneous grains in terms of the composition and the shape. Such a possibility is modelled by Mathis & Whiffen (1989), who constructed a model of interstellar grains that are assumed to be aggregates of multiple species containing vacuum. They succeeded in obtaining a model that is consistent with the observed Milky Way extinction curves. Although composite aggregates (composed of multiple grain species) could be disrupted into single species in the diffuse ISM (Li & Greenberg 1997; Hoang 2019), it is at least expected that coagulation develops non-sphericity with vacuum, which could lead to porous (or fluffy) grains.

Indeed, fluffy large grains are observationally indicated by the X-ray scattering halos surrounding point sources, such as X-ray binaries (Woo et al. 1994) and Nova Cygni 1992 (Mathis et al. 1995). Mathis et al. (1995) attempted to reproduce the X-ray halo strength of Nova Cygni 1992 under the observed optical extinction towards that object. Smith & Dwek (1998) reconsidered the treatment of grain optical properties using the Mie solution, and concluded, contrary to the above conclusion, that compact silicate and carbon grains are consistent with the observation of the X-ray scattering halo around Nova Cygni 1992. Draine & Tan (2003) also indicated that a compact-grain model based on Weingartner & Draine (2001b) is consistent with the dust towards Nova Cygni 1992 if a lower optical extinction is adopted. Draine (2003) also discussed the X-ray halo of Cyg X-1 in addition to that of Nova Cygni 1992 and supported the same compact-grain model; however, they also mentioned the uncertainty arising from the distribution of dust in the line of sight. Within the uncertainty, grains with moderate porosities could still exist in the diffuse ISM

Considering porous grains was also motivated by the severe constraint on the available metals (especially carbon) historically. Mathis (1996) investigated a possibility of reproducing the Milky Way extinction curve with fluffy grains. As a consequence, they 'saved' the heavy elements the most (i.e. used the minimum amount of metals for dust) by including 25–65 per cent of vacuum in the dust grains. Very fluffy grains are excluded because their extinction (absorption + scattering) per unit dust mass is too low. However, Dwek et al. (1997) argued that, if we take the fitting to the infrared dust emission SED into account, Mathis (1996)'s model overproduces the optical–ultraviolet (UV) extinction. Li (2005) showed, based on the argument on the Kramers-Kronig relations, that the observed optical–UV extinction is still underproduced with the Galactic metal abundance derived from B stars. We should also keep in mind that recent dust models with updated extinction-to-column density ratios (A_V/N_H) and the protosolar abundance with a correction for Galactic chemical evolution after the Sun formation indicate that the above severe metallicity constraint may not be an issue any more (Draine & Hensley 2020; Hensley & Draine 2020; Zuo et al. 2020).

Clarifying how porous the interstellar dust could be is in itself a problem independent of the metal abundance constraint. Since the above mentioned studies did not necessarily give a definite constraint on the grain porosity, it is still meaningful to investigate the effect of porosity on the extinction curves in a general context. Voshchinnikov et al. (2005, 2006) studied the dependence of extinction curve on the porosity. These studies give a basis on which we constrain the allowed ranges of porosity through comparison with observations. In reality, porosity could depend on the grain size, because the evolution of grain size distribution plays an important role in determining the grain porosity. However, it is difficult to relate grain size and porosity, since the physical link between these two quantities is still missing. Because of this 'missing link', the poros-

ity still remains to be a free parameter. It is definitely necessary to understand the interplay between grain size and porosity in the evolution of interstellar dust, if we would like to obtain a meaningful insight into the physical mechanisms of dust evolution through the observationally constrained grain porosities.

The evolution of porous grains by coagulation has been modelled and discussed in the field of protoplanetary discs. Ormel et al. (2007) developed a Monte Carlo method for the evolution of grain size distribution by coagulation in protoplanetary discs taking the porosity evolution into account. In each collision, depending on the collision energy, they treated the difference between the hit-and-stick (sticking without modifying the grain shapes) and compaction (decrease of grain volume by compression) regimes. Okuzumi et al. (2009, hereafter O09) formulated this problem by using the 2-dimensional (2D) Smoluchowski equation that treats distribution function of two variables, grain radius and porosity. Since directly solving the 2D equation is computationally expensive, they only concentrated on the mean porosity at each grain radius while they fully solved the grain size distribution (see also Okuzumi et al. 2012, hereafter O12). They finally obtained a set of moment equations for the grain volume: the zeroth order describes the grain size distribution and the first order the 'grain volume distribution'. A set of grain radius and grain volume gives information on the grain porosity. The calculated porosity is also useful to predict the radiative properties of dust grains in protoplenetary discs (e.g. Kataoka et al. 2014; Tazaki et al. 2016).

The above methods to trace the evolution of porous grains are applied to the grain evolution in dense molecular clouds. Ormel et al. (2009) applied the above mentioned Monte Carlo method (but including also grain fragmentation) and showed that the filling factor of grain could become as small as ∼ 0.1 (i.e. the fraction of vacuum is ∼ 0.9). Since the optical properties of dust could be affected by grain porosity, modelling of porosity is important in interpreting the wavelength dependence of absorption and emission in dense molecular clouds (Ormel et al. 2011; Lefèvre et al. 2020). However, these works mainly consider dense ($\gtrsim 10^4$ cm^{-3}) environments, and the relation to the grains actually contributing to the interstellar extinction is not clear. As mentioned above, shattering is also important as a modifying mechanism of grain size distribution. The functional shape of the grain size distribution could be determined by the balance between shattering and coagulation. This balance could also be important to determine the porosities at various grain sizes.

The goal of this paper is to clarify the evolution of porous grains in the ISM by considering both coagulation and shattering. We have already formulated the evolution of grain size distribution using the Smoluchowski equation in our previous works (e.g. Hirashita & Yan 2009; Asano et al. 2013; Hirashita & Aoyama 2019). For the porosity evolution, we utilize the framework developed by O09 and O12 for protoplanetary discs with some modifications mainly to include shattering. Our model developed in this paper is aimed at being used to calculate the dust evolution on galaxy scales in the future. Although the Smoluchowski equation usually refers to the one describing coagulation, we broadly use this name also for an extended version for shattering.

As a result of the modelling in this paper, we will be able to predict the expected grain porosity as a function of grain radius in the ISM. We emphasize that the previous models of grain porosity introduced above mostly treated porosity as a free parameter to be fitted to observed dust properties such as extinction curves. Thus, this study will provide the first prediction on the grain-radius-dependent porosity expected theoretically from coagulation and shattering. We also calculate extinction curves to clarify the effect of predicted porosity on an observable dust property. This paper is not aimed

at complete modelling but focused on the construction of a basic framework for clarifying how large the porosity could be in the presence of coagulation and shattering.

This paper is organized as follows. In Section 2, we formulate the evolution of grain size distribution and porosity. We show the results in Section 3, and present the effects on extinction curves in Section 4. We provide some extended discussions, especially focusing on the effects of porosity in Section 5. We give the conclusion of this paper in Section 6.

2 MODEL

First of all, we clarify some terms. The *filling factor* of a grain is defined as the volume fraction occupied by the material composing the grain. The rest (unity minus the filling factor) is referred to as the *porosity*, which is the volume fraction of vacuum. A grain is *compact* if the filling factor is unity (i.e. no porosity). In our previous papers (e.g. Hirashita & Aoyama 2019) and others (e.g. Jones et al. 1994, 1996; Mattsson 2016), the evolution of grain size distribution in the ISM is formulated for compact grains. Here, we extend the formulation to include the evolution of grain porosity.

As mentioned in the Introduction, we concentrate on the collisional processes for grain evolution, namely coagulation and shattering, since they are the main drivers for the evolution of both grain size distribution and grain porosity. We neglect dust evolution processes other than coagulation and shattering. This treatment assumes that coagulation and/or shattering occur in a 'closed box' without any supply from stellar dust production and from accretion of gas-phase metals, and without any loss of dust by supernova shock destruction. For simplicity, we consider a single dust species in solving the evolution of grain size distribution and porosity to avoid the complexity arising from compound species. That is, we concentrate on the effect of porosity in a single dust species.

Coagulation and shattering occur in the different ISM phases (dense and diffuse ISM phases, respectively). However, since the exchange of these phases occurs on a short time-scale ($\sim 10^7$ yr; McKee 1989), we consider the mixture of coagulation and shattering in addition to treating each process separately. For the dense and diffuse ISM phases, we consider representative phases that could affect the major dust populations in the ISM and the physical conditions are given in Section 2.5. The grain motions are assumed to be driven by interstellar turbulence. We do not trace coagulation in a star-forming cloud with densities $\gtrsim 10^4$ cm^{-3}, since, as mentioned in the Introduction, the relation of the grains formed in such extreme environments to the general ISM grains is not clear. Moreover, we need to consider physical processes such as ambipolar diffusion in considering the grain motion in star-forming clouds (e.g. Silsbee et al. 2020; Guillet et al. 2020). Therefore, we leave the detailed studies of dense star-forming clouds for a future work.

Coagulation in the dense ISM could be complex since accretion of gas-phase materials could occur at the same time (Hirashita & Voshchinnikov 2014; Voshchinnikov & Hirashita 2014). Accretion could decrease the porosity because part of the vacuum could be filled (Li & Lunine 2003, appendix B). As a result of accretion in an environment where UV radiation is shielded, ice mantles could also develop on the grain surfaces. However, such mantles are evaporated in the diffuse ISM so that aggregates attached through the ice mantles could dissolve once they are injected into the diffuse ISM. As mentioned later, whether or not ice mantles enhance coagulation is still debated, and refractory surfaces could be more sticky (Section 2.3.1). Therefore, it is hard to clarify with the cur-

rently available knowledge how ice mantles affect the observed grain properties (e.g. extinction curves) in the ISM through coagulation. Since we are interested in the general population of grains in the ISM (especially, silicate and carbonaceous dust), we neglect the formation of volatile mantles, and assume that the collisions between refractory grains in the dense ISM lead to formation of refractory coagulated grains. We also neglect the possible development of core-mantle structures as a result of accretion, which could explain the Milky Way dust properties (Li & Greenberg 1997; Jones et al. 2017). We simply examine the effect of porosity on the extinction curves of basic materials (silicate and carbonaceous dust in this paper; Section 2.4), but do not aim at reproducing the observed Milky Way extinction curve.

In this paper, we also neglect the electric charge of grains. The grain collision cross-section could be enhanced or reduced depending on the grain charge. The charge effect is not important for large grains because they have high kinetic energy (i.e. the Coulomb force does not alter the grain motion) as commented in Hirashita & Aoyama (2019). The charge may be important for coagulation of small grains, which are positively or negatively charged depending on the physical condition of the ambient medium and radiation field (Weingartner & Draine 2001a). For example, in a physical condition appropriate for molecular clouds, small grains tend to be charged negatively, while large grains positively (Yan et al. 2004). This situation could suppress the collisions between small grains but enhance those between a small and a large grain. At the same time, the grain charge is very sensitive to the assumed physical conditions in the dense clouds (especially, the ionization degree and the UV radiation field intensity, which is affected by the dust attenuation). Although it is interesting to investigate the detailed dependence on these physical parameters, in this paper we choose to neglect the effect of grain charge for the simplicity of our treatment.

2.1 Basic framework

The evolution of grain size distribution and grain porosity by coagulation is formulated by O09 and O12. Although their main target was dust evolution in protoplanetary discs, the generality of their formulation allows us to apply it to interstellar dust. We also include shattering in this paper. The evolution of grain size distribution and grain porosity by coagulation and shattering is described by the distribution functions of grain mass (m) and grain volume (V)[1] at time t, and is governed by the 2D Smoluchowski equation. However, as noted by O09, solving the 2D Smolchowski equation requires a huge computational expense. Therefore, we concentrate on the moment equations for V, but we still solve the full distribution function for m.

To treat porous grains, it is convenient to introduce the following two types of grain radius: characteristic radius (a_{ch}) and mass-equivalent radius (a_m). The characteristic radius is related to the volume as $V = (4\pi/3)a_{ch}^3$, while the mass-equivalent radius is related to the grain mass as $m = (4\pi/3)a_m^3 s$, where s is the bulk material density. For compact grains, $m = sV$, so that $a_{ch} = a_m$. For porous grains, $a_{ch} > a_m$. Using these two grain radii, the filling factor, ϕ_m, is expressed as $\phi_m \equiv (a_m/a_{ch})^3 (\leq 1)$ (see also Ormel et al. 2009), while the porosity is $1 - \phi_m$. Since it is necessary to specify s, we simply adopt the same value as used in HM20 ($s = 2.24$ g cm^{-3} taken from graphite), but adopting $s = 2$–3.5 g cm^{-3} appropriate for interstellar grains (e.g. Weingartner & Draine 2001b) does not

---

[1] We use the upper case V for volumes and the lower case v for velocities throughout this paper.

change our conclusion significantly. We vary some parameters relevant for porosity, which are more important in this paper (Section 2.5). Thus, we simply use the same parameters as in HM20 for the material properties (specifically s and $Q_D^\star$ introduced later) that do not directly affect the porosity evolution.

Before presenting the basic equations, we need to introduce some quantities. We use the grain mass distribution instead of the grain size distribution since there is ambiguity in the grain size for porous grains. We denote the distribution function of m and V at time t as $f(m, V, t)$. The grain mass distribution at time t, $\tilde{n}(m, t)$ is defined such that $\tilde{n}(m, t)\,\mathrm{d}m$ is the number density of grains whose mass is between m and $m + \mathrm{d}m$, and is related to the above distribution function as

$$\tilde{n}(m, t) \equiv \int_0^\infty f(m, V, t)\,\mathrm{d}V. \tag{1}$$

We also introduce the first moment of f for V as

$$\bar{V}(m, t) \equiv \frac{1}{\tilde{n}(m, t)} \int_0^\infty V f(m, V, t)\,\mathrm{d}V. \tag{2}$$

This quantity ($\bar{V}$) is the mean volume of grains with mass m. We define the following two quantities, $\rho(m, t) \equiv m\tilde{n}(m, t)$ and $\psi(m, t) \equiv \bar{V}(m, t)\tilde{n}(m, t)$, which represent the grain mass distribution weighted for the grain mass and volume, respectively (the latter can also be regarded as the volume distribution function). The integration of $\rho(m, t)$ for m is related to the dust-to-gas ratio, $\mathcal{D}$, as

$$\mu_H m_H n_H \mathcal{D} = \int_0^\infty \rho(m, t)\,\mathrm{d}m, \tag{3}$$

where $\mu_H = 1.4$ is the gas mass per hydrogen, m_H is the hydrogen atom mass, and n_H is the hydrogen number density.

The Smolchowski equation contains the collision kernel, which is the product of the collision cross-section and the relative speed of colliding pair. The collision kernel for colliding grains with masses m_1 and m_2 is denoted as K_{m_1, m_2}, which is evaluated in Section 2.2.

It is straightforward to derive the following general equations applicable for both coagulation and shattering based on equations (6) and (7) of O09:

$$\frac{\partial \rho(m, t)}{\partial t} = -m\rho(m, t) \int_0^\infty \frac{K_{m, m_1}}{m m_1} \rho(m_1, t)\mathrm{d}m_1$$
$$+ \int_0^\infty \int_0^\infty \frac{K_{m_1, m_2}}{m_1 m_2} \rho(m_1, t)\rho(m_2, t) m\bar{\theta}(m; m_1, m_2)\mathrm{d}m_1\mathrm{d}m_2, \tag{4}$$

$$\frac{\partial \psi(m, t)}{\partial t} = -\bar{V}(m, t)\psi(m, t) \int_0^\infty \frac{K_{m, m_1}}{\bar{V}(m, t)\bar{V}(m_1, t)} \psi(m_1, t)\mathrm{d}m_1$$
$$+ \int_0^\infty \int_0^\infty \frac{K_{m_1, m_2}}{\bar{V}(m_1)\bar{V}(m_2)} \psi(m_1, t)\psi(m_2, t)(V_{1+2})_{m_1, m_2}^m \bar{\theta}(m; m_1, m_2)\mathrm{d}m_1\mathrm{d}m_2, \tag{5}$$

where $\bar{\theta}(m; m_1, m_2)$ describes the distribution function of grains produced from m_1 in the collision between grains with masses m_1 and m_2, and $(V_{1+2})_{m_1, m_2}^m$ is the volume of the newly produced grain with mass m in the above collision. Since the expression is not exactly the same as that used by O09 and O12, we explain the derivation of the above equations in Appendix A. In particular, in our formulation, we count the collisional products originating from m_1 and m_2 separately. O09, in contrast, considered the collisional pair m_1 and m_2 only once. This is why O09 has a factor 1/2 in front of the second term on the right-hand side in equations (4) and (5).

We aim at solving equations (4) and (5) for ρ and ψ. Since $\rho/m = \psi/\bar{V}$ is always satisfied, $\bar{V}$ is not an independent quantity. Thus, these

two equations are closed if we give K, V_{1+2} and $\bar{\theta}$. In the following subsections, we explain how to determine these three quantities.

In computing the grain size distribution, we discretize the entire grain radius range ($a = 3 \times 10^{-4}$–10 μm) into 128 grid points with logarithmically equal spacing. We set $\rho_d(m, t) = 0$ at the maximum and minimum grain radii for the boundary conditions. We use the algorithm described in appendix B of Hirashita & Aoyama (2019) to solve the discretized equations.

2.2 Collision kernel

The collision kernel is determined by the product of the grain cross-section and the relative velocity. The cross-section ($\sigma_{1,2}$) in the collision of grains with masses m_1 and m_2, referred to as grain 1 and 2, respectively, is estimated as $\sigma_{1,2} = \pi(a_{ch1} + a_{ch2})^2$, where the characteristic radii of grains 1 and 2 are a_{ch1} and a_{ch2}, respectively (see the beginning of Section 2.1 for the definition of the characteristic radius; i.e. $a_{ch} = a_m \phi_m^{-1/3}$).

The motion of dust grains is assumed to be induced by turbulence (e.g. Kusaka et al. 1970; Voelk et al. 1980). We basically adopt the same simple model, originally taken from Ormel et al. (2009), for the grain velocity v_{gr} as adopted in our previous papers:

$$v_{gr}(m) = 1.1\mathcal{M}^{3/2}\phi_m^{1/3} \left(\frac{a_m}{0.1\ \mu m}\right)^{1/2} \left(\frac{T_{gas}}{10^4\ K}\right)^{1/4} \left(\frac{n_H}{1\ cm^{-3}}\right)^{-1/4}$$
$$\times \left(\frac{s}{3.5\ g\ cm^{-3}}\right)^{1/2}\ km\ s^{-1}, \tag{6}$$

where $\mathcal{M}$ is the Mach number of the largest-eddy velocity, and T_{gas} is the gas temperature. This is similar to equation (18) of Hirashita & Aoyama (2019), but modified to include the filling factor ϕ_m (see appendix A of Ormel et al. 2009). The derivation of the above equation does not strictly hold for highly supersonic regime, but we practically use $\mathcal{M}$ here as an adjusting parameter for the grain velocity. Under fixed ISM conditions and grain material properties, the velocity is reduced to a function of m. Since the filling factor ϕ_m changes as a function of time, $v_{gr}(m)$ also varies with time. In considering the collision rate between grains 1 and 2 with $v_{gr}(m_1) = v_1$ and $v_{gr}(m_2) = v_2$, we estimate the relative velocity $v_{1,2}$ by

$$v_{1,2} = \sqrt{v_1^2 + v_2^2 - 2v_1 v_2 \mu_{1,2}}, \tag{7}$$

where $\mu = \cos\theta$ (θ is an angle between the two grain velocities) is randomly chosen between -1 and 1 in every calculation of the collision kernel (Hirashita & Li 2013).

Using the above quantities, the collision kernel is estimated for the collision between grains 1 and 2 as

$$K_{m_1, m_2} = \sigma_{1,2} v_{1,2}. \tag{8}$$

Note that the collision kernel depends on the filling factor of the larger grain as $\propto \phi_m^{-1/3}$. Thus, the grain–grain collision rate is enhanced if the grains become more porous (fluffy).

2.3 Treatment of grains produced by collisions

The treatment of collisional products is the key for the evolution of porosity. The porosity is strongly affected by the production of vacuum volume in a grain after grain–grain sticking (coagulation) and the compaction associated with compression in grain–grain collisions. However, these processes are strongly nonlinear and dependent on the actual grain shapes. Moreover, some assumptions in O09 and

O12 are not applicable to interstellar dust. In particular, their formulation is based on single-sized ($\sim 0.1\ \mu$m) monomers, since they are interested in protoplanetary discs, where grains grow into much larger sizes than interstellar grains. In the ISM, in contrast, we also consider the evolution of grains much smaller than the 'typical' grain size ($\sim 0.1\ \mu$m). To make the problem more complicated, shattering also occurs, producing a large number of small grains. Because of the above difficulty and the difference from O09 and O12, we take the following approach that simplifies the treatment of porosity evolution but still preserves the essence of physical processes regarding grain–grain sticking and compression.

2.3.1 Coagulation

For coagulation, two characteristic energies are important: impact (kinetic) energy and the rolling energy. The impact energy ($E_{\rm imp}$) in the collision between grains 1 and 2 is estimated as

$$E_{\rm imp} = \frac{1}{2}\frac{m_1 m_2}{m_1 + m_2} v_{1,2}^2 . \tag{9}$$

The rolling energy ($E_{\rm roll}$) is defined as the energy necessary for a monomer to roll over 90 degrees on the surface of another monomer (Dominik & Tielens 1997), and is given by (Wada et al. 2007)

$$E_{\rm roll} = 12\pi^2 \gamma R_{1,2} \xi_{\rm crit}, \tag{10}$$

where γ is the surface energy per unit contact area, $R_{1,2}$ is the reduced particle radius, and $\xi_{\rm crit}$ is the critical displacement of rolling. The surface energy depends on the surface material: γ = 25, 75, and 100 erg cm^{-2} for silicate (originally from quartz), graphite, and water ice, respectively (Dominik & Tielens 1997; Israelachvili 1992; Wada et al. 2007). The critical displacement $\xi_{\rm crit}$ lies broadly in the range of $\sim$2–30 Å (Dominik & Tielens 1997; Heim et al. 1999; Wada et al. 2007). As shown by Kimura et al. (2015) and Steinpilz et al. (2019), the surface energy of dry silica could be larger than the above values. This implies that the above surface energy for silicate is underestimated. Since γ and $\xi_{\rm crit}$ are degenerate, we fix γ to an intermediate value (75 erg cm^{-2}) and vary $\xi_{\rm crit}$. We choose a fiducial value $\xi_{\rm crit} = 10$ Å unless otherwise stated but we later examine a case where $\xi_{\rm crit}$ is varied.

The reduced radius, $R_{1,2}$, is difficult to determine rigidly for interstellar dust, since the typical monomer size is not obvious. Thus, we simply assume that

$$\frac{1}{R_{1,2}} = \frac{1}{a_{m_1}} + \frac{1}{a_{m_2}}. \tag{11}$$

This equation gives a reasonable estimate for $R_{1,2}$ for compact grains. As shown later, small grains tend to be compact. Since the reduced radius is dominated by the smaller grain, the above estimate could be justified. Large (submicron/micron) grains are also affected by compaction, so that the above reduced radius could be applied for collisions between large grains. However, the above reduced mass may be overestimated in collisions between porous grains. Grains with intermediate radii ($a \sim 0.01$–$0.1\ \mu$m) tend to be porous. Overestimation of $R_{1,2}$ leads to less efficient compaction. On the other hand, the uncertainty in $R_{1,2}$ could be absorbed by the variation of $\xi_{\rm crit}$ and $n_{\rm c}$ ($n_{\rm c}$ is introduced below). Thus, we vary $\xi_{\rm crit}$ and $n_{\rm c}$ to effectively investigate the uncertainties caused by collisions between intermediate-sized grains.

We now estimate the volume of the coagulated grain. We do not directly adopt O12's formulation (their equation 15; see also Suyama et al. 2012) because, as mentioned above, the monomer size is not well determined for interstellar dust. Nevertheless, we apply the

following essential points (Dominik & Tielens 1997): (i) The physical outcome of the collision is characterized by the ratio between $E_{\rm imp}$ and $E_{\rm roll}$. (ii) If $E_{\rm imp} \ll E_{\rm roll}$, the grains stick without modifying their structures (hit-and-stick collisions). (iii) If $E_{\rm imp} \sim E_{\rm roll}$, the newly added void tends to be compressed because the contact points of monomers are moved. (iii) If $E_{\rm imp} \gtrsim n_{\rm c} E_{\rm roll}$, where $n_{\rm c}$ is the number of contact points, significant compaction occurs. Since we do not trace each monomer, $n_{\rm c}$ is uncertain. Moreover, not all contact points are equally important in compaction. Thus, we treat $n_{\rm c}$ as a free parameter, and regard it as the number of major contacts whose movement contributes to compaction significantly. Since $n_{\rm c}$ always appears in the form of product $n_{\rm c} E_{\rm roll}$, $n_{\rm c}$ is degenerate with $E_{\rm roll}$ as mentioned above. Considering the above three points, (i)–(iii), we estimate the volume (V_{1+2}^0) of coagulated product in the collision between grains with volumes V_1 and V_2 (assuming that $V_1 \geq V_2$; if $V_1 < V_2$, we exchange grains 1 and 2, so that the following formulation holds) as

$$V_{1+2}^0 = V_1 + V_2 + V_{\rm void} \exp\left[-E_{\rm imp}/(3bE_{\rm roll})\right]$$
$$+ (V_{2,\rm comp} - 2V_2)\left\{1 - \exp\left[-E_{\rm imp}/(n_{\rm c}E_{\rm roll})\right]\right\}, \tag{12}$$

where $V_{\rm void}$ is the volume of the void newly created in the collision, $b = 0.15$ is an adjusting parameter (Wada et al. 2008), and $V_{2,\rm comp} \equiv m_2/s$ (the volume with perfect compaction). The void volume is estimated as (O12)

$$V_{\rm void} = \min\left[0.99 - 1.03\ln\left(\frac{2}{V_1/V_2 + 1}\right),\ 6.94\right]V_2. \tag{13}$$

Equation (12) satisfies the above conditions (i)–(iii): $V_{1+2}^0 \simeq V_1 + V_2 + V_{\rm void}$ for $E_{\rm imp} \ll E_{\rm roll}$. The newly created volume ($V_{\rm void}$) is compressed if $E_{\rm imp} \gtrsim E_{\rm roll}$. If $E_{\rm imp}$ becomes comparable to or higher than $n_{\rm c} E_{\rm roll}$, the grain is compressed further (note that $V_{2,\rm comp} - 2V_2 \leq 0$). If $E_{\rm imp} \gg n_{\rm c}E_{\rm roll}$, $V_{1+2}^0 = (V_1 - V_2) + V_{2,\rm comp}$ (note that $V_1 \geq V_2$), which means that V_2 becomes compact while V_1 is compressed by the equivalent volume to V_2. According to Wada et al. (2013), in a collision of grains with different sizes, the larger grain is not entirely compressed. We assume that the compressed volume in the larger grain is determined by the volume of the smaller grain. In the above expression, V_{1+2}^0 can be smaller than $V_{1,\rm comp} + V_{2,\rm comp}$, where $V_{1,\rm comp} = m_1/s$ (the volume with perfect compaction). Thus, we finally adopt the following expression for the coagulated volume, V_{1+2}:

$$V_{1+2} = \begin{cases} V_{1+2}^0 & \text{if } V_{1+2}^0 > V_{1,\rm comp} + V_{2,\rm comp}, \\ (1+\epsilon_V)(V_{1,\rm comp} + V_{2,\rm comp}) & \text{otherwise}, \end{cases} \tag{14}$$

where $\epsilon_V \geq 0$ is a parameter reflecting the fact that perfect compaction is difficult (Suyama et al. 2012; Wada et al. 2013). We use this volume for $(V_{1+2})_{m_1,m_2}^m$ in equation (5).

The mass distribution of collisional products is described by (see equation 26 of Hirashita & Aoyama 2019)

$$m\bar\theta(m; m_1, m_2) = m_1\delta[m - (m_1 + m_2)], \tag{15}$$

where $\delta(\cdot)$ is Dirac's delta function. As mentioned above and in Appendix A, we separately treat the collision product originating from m_1 and that from m_2 (i.e. we count the same collision twice).

2.3.2 Shattering

There has not been any formulation for the evolution of porosity by shattering in the ISM. Shattering produces a lot of fragments, and sometimes leaves a remnant if the original grain is much larger

than the colliding partner. We expect that shattered fragments have small porosities because weakly bound parts become unbound in disruptive collisions. Thus, we assume that the collisional fragments are compact. For the remnant, it is probable compaction occurs; however, in our formulation, the remnant remains only if a grain collides with a much smaller grain: in this case, it is not clear if the entire remnant is efficiently pressed. Thus, we simply assume that the shattered remnant has the same porosity as the original grain. We examine separately a case where we take compaction of the remnants into account.

The microscopic processes for shattering of porous grains in high-velocity ($\gtrsim 1 \, \mathrm{km \, s^{-1}}$) collisions are not well known. Moreover, in our formulation, we have to treat collisions of both porous and compact grains. Thus, we use our previous formulation in Hirashita & Aoyama (2019), which is appropriate for compact grains. We also expect that the resulting grain size distribution is not sensitive to detailed assumptions on the fragment size distribution (Hirashita & Kobayashi 2013). We explain the treatment of shattered fragments in what follows.

We consider a collision of two dust grains with masses m_1 and m_2 (grains 1 and 2) based on Kobayashi & Tanaka (2010)'s model. The ejected mass (m_{ej}) from grain 1 is estimated as

$$m_{\mathrm{ej}} = \frac{\varphi}{1 + \varphi} m_1, \tag{16}$$

with

$$\varphi \equiv \frac{E_{\mathrm{imp}}}{m_1 Q_{\mathrm{D}}^{\star}}, \tag{17}$$

where $Q_{\mathrm{D}}^{\star}$ is the specific impact energy required to disrupt half of the mass ($m_1/2$). We adopt $Q_{\mathrm{D}}^{\star} = 8.9 \times 10^9 \, \mathrm{erg \, g^{-1}}$ following HM20. The ejected mass is distributed into fragments, for which we assume a power-law size distribution with an index of $\alpha_{\mathrm{f}} = 3.3$ (Jones et al. 1996). This index is translated into that of $\bar{\theta}$ as $\bar{\theta} \propto m^{-(\alpha_{\mathrm{f}}+2)/3}$. The maximum and minimum masses of the fragments are assumed to be $m_{\mathrm{f,max}} = 0.02 m_{\mathrm{ej}}$ and $m_{\mathrm{f,min}} = 10^{-6} m_{\mathrm{f,max}}$, respectively (Guillet et al. 2011). We adopt the following mass distribution function of collisional product from grain 1 in the collision with grain 2 as

$$m\bar{\theta}(m, m_1, m_2) = \frac{(4 - \alpha_{\mathrm{f}}) m_{\mathrm{ej}} m^{(-\alpha_{\mathrm{f}}+1)/3}}{3 \left[m_{\mathrm{f,max}}^{\frac{4-\alpha_{\mathrm{f}}}{3}} - m_{\mathrm{f,min}}^{\frac{4-\alpha_{\mathrm{f}}}{3}} \right]} \Phi(m; m_{\mathrm{f,min}}, m_{\mathrm{f,max}})$$
$$+ m\delta(m - m_1 + m_{\mathrm{ej}}), \tag{18}$$

where $\Phi(m; m_{\mathrm{f,min}}, m_{\mathrm{f,max}}) = 1$ if $m_{\mathrm{f,min}} \leq m \leq m_{\mathrm{f,max}}$, and 0 otherwise. Grains which become smaller than the minimum grain size ($a_m = 3 \times 10^{-4} \, \mu\mathrm{m}$) are removed. For the volumes of shattered products, we adopt

$$V_{1+2} = \begin{cases} \bar{V}(m_1)/(1 + \varphi) & \text{if } m = m_1 - m_{\mathrm{ej}} = m_1/(1 + \varphi), \\ m/s & \text{otherwise.} \end{cases} \tag{19}$$

The first case of this expression indicates that the porosity (or filling factor) of the remnant is the same as that of the original grain. The second case means that the fragments are compact (that is, the volumes are simply estimated by the mass divided by the material density). We use equation (19) for $(V_{1+2})_{m_1,m_2}^m$ in equation (5).

2.4 Calculation of extinction curves

To investigate the effects on observed dust properties, we also calculate extinction curves. We examine two representative grain materials: silicate and carbonaceous species, and investigate how the

porosity evolution driven by coagulation and shattering affects the extinction properties of these materials. For silicate, we use the optical constants of astronomical silicate adopted by Weingartner & Draine (2001b). For carbonaceous dust, we adopt amorphous carbon (amC) from 'ACAR' in Zubko et al. (1996). Graphite is another possible carbonaceous material, and we confirmed that it produces similar results to amC except at wavelengths where the 2175 Å feature is prominent. We also found that the wavelength where the feature peaks shifts with the porosity, but such a shift is not observed in the Milky Way extinction curves. Thus, special care should be taken of the modelling of the 2175 Å feature, e.g. by treating the 2175 Å carrier such as graphite and PAHs (e.g. Li & Draine 2001) as a component separated from porous grain species (Voshchinnikov et al. 2006), which is out of the scope of this paper. Thus, we adopt amC in this paper, noting that, as mentioned above, amC and graphite produce similar results at wavelengths not affected by the 2175 Å feature.

The optical properties of dust is calculated using the effective medium theory (EMT), which averages the dielectric permittivity using a mixing rule. We adopt the Bruggeman mixing rule. This mixing rule as well as the Garnett mixing rule gives reasonable extinctions as long as the grains do not have substructures (e.g. monomers) larger than the wavelength (Voshchinnikov et al. 2005). As shown later, the porous grains are formed by coagulation of grains smaller than $\sim 0.1 \, \mu\mathrm{m}$ and we are interested in wavelengths longer than 0.1 $\mu\mathrm{m}$. Thus, the above condition is satisfied in this paper. Even if we model the inhomogeneity using multi-layered spheres, the difference in the extinction is expected to be less than ~ 10 per cent (Voshchinnikov et al. 2005; Shen et al. 2008). Using the Bruggeman mixing rule, the averaged dielectric permittivity $\bar{\varepsilon}$ is obtained from

$$(1 - \phi_m)\frac{1 - \bar{\varepsilon}}{1 + 2\bar{\varepsilon}} + \phi_m \frac{\varepsilon_2 - \bar{\varepsilon}}{\varepsilon_2 + 2\bar{\varepsilon}} = 0, \tag{20}$$

where ε_2 is the dielectric permittivity of the material (note that the first material is assumed to be vacuum so $\varepsilon_1 = 1$).[2] We assume that each dust grain is a sphere with radius a_{ch} and refractive index $\bar{m} = \sqrt{\bar{\varepsilon}}$. The cross-section $C_{\mathrm{ext},m}$, which is a function of m under a given ϕ_m at each epoch, is calculated by the Mie theory (Bohren & Huffman 1983).

The extinction at wavelength λ in units of magnitude (A_λ) can be calculated using the grain size distribution as

$$A_\lambda = (2.5 \log_{10} e)L \int_0^\infty \tilde{n}(m) \, C_{\mathrm{ext},m} \, \mathrm{d}m, \tag{21}$$

where 'L' is the path length. We present the extinction in the following two ways: A_λ/N_{H} and A_λ/A_V (the V band wavelength corresponds to $\lambda^{-1} = 1.8 \, \mu\mathrm{m}^{-1}$ and $N_{\mathrm{H}} = n_{\mathrm{H}} L$ is the column density of hydrogen nuclei). The first quantity indicates the extinction per hydrogen (thus, it is proportional to the dust abundance), while the second is useful to show the shape of extinction curve. In both quantities, the path length L is canceled out.

2.5 Parameter settings

Coagulation and shattering are governed by the same form of equation (equations 4 and 5). These two processes occur in different ISM phases. We assume that coagulation occurs in the dense clouds of which the physical conditions are described by $n_{\mathrm{H}} = 10^3 \, \mathrm{cm}^{-3}$ and $T_{\mathrm{gas}} = 10$ K (typical of molecular clouds); and that shattering takes place in the diffuse ISM characterized by $n_{\mathrm{H}} = 0.3$

---

[2] We adopt Gaussian-cgs units.

cm^{-3} and $T_{\text{gas}} = 10^4$ K. These values are similar to the ones adopted for coagulation and shattering by Hirashita & Yan (2009). The density affects the grain collision time-scale, which scales with $(n_H v_{\text{gr}})^{-1} \propto n_H^{-3/4}$ (see equation 6); that is, the adopted duration for shattering/coagulation is degenerate with the gas density. Therefore, we fix the above physical conditions for the gas and examine the grain size distributions at various times (i.e. for various durations of the process), keeping in mind that the same value of $n_H^{3/4} t$ gives similar results.

For the normalization of the grain velocities adjusted by $\mathcal{M}$ in equation (6), we apply $\mathcal{M} = 3$ for shattering and $\mathcal{M} = 1$ for coagulation (HM20). These values of $\mathcal{M}$ are adopted to obtain a similar level of grain velocities to those calculated for magnetized turbulence by Yan et al. (2004).

We not only treat shattering and coagulation separately, but also examine some cases where these two processes occur at the same time. The coexistence of shattering and coagulation is a reasonable approximation for a volume of the ISM wide enough to sample a statistically significant amount of both ISM phases and/or for a time much longer than the mixing time-scale of the two ISM phases ($\sim 10^7$ yr; e.g. McKee 1989). Since coagulation and shattering occur in the media with different densities, it is convenient to define the grain mass and volume distributions per hydrogen number density as $\tilde{\rho} \equiv \rho/n_H$ and $\tilde{\psi} \equiv \psi/n_H$, respectively. In this case, we calculate the evolution of $\tilde{\rho}$ and $\tilde{\psi}$ by

$$\left.\frac{\partial \tilde{\rho}(m,t)}{\partial t}\right|_{\text{tot}} = \eta_{\text{dense}} \left.\frac{\partial \tilde{\rho}(m,t)}{\partial t}\right|_{\text{coag}} + (1-\eta_{\text{dense}}) \left.\frac{\partial \tilde{\rho}(m,t)}{\partial t}\right|_{\text{shat}},$$ (22)

$$\left.\frac{\partial \tilde{\psi}(m,t)}{\partial t}\right|_{\text{tot}} = \eta_{\text{dense}} \left.\frac{\partial \tilde{\psi}(m,t)}{\partial t}\right|_{\text{coag}} + (1-\eta_{\text{dense}}) \left.\frac{\partial \tilde{\psi}(m,t)}{\partial t}\right|_{\text{shat}},$$ (23)

where η_{dense}, which is treated as a free parameter, is the dense gas fraction determining the weight of each process, the subscript 'tot' indicates the total changing rates of $\tilde{\rho}$ and $\tilde{\psi}$, and the subscripts 'coag' and 'shat' mean the changes caused by coagulation and shattering, respectively. For the two terms on the right-hand side of the above equations, we apply equations (4) and (5). The change by coagulation and that by shattering are mixed with a ratio of $\eta_{\text{dense}} : (1-\eta_{\text{dense}})$; in other words, η_{dense} determines the fraction of time dust spends in the dense ISM. In calculating shattering and coagulation, we use ρ and ψ, but when we sum up the contributions from coagulation and shattering, we divide them by n_H and obtain $\tilde{\rho}$ and $\tilde{\psi}$. Here we implicitly neglect gas which hosts neither coagulation nor shattering. Existence of such a gas component effectively lowers the efficiencies of both shattering and coagulation (or makes the time-scales of these two processes longer) equally and does not affect the relative roles of these two processes.

2.5.1 Important parameters specific for coagulation

As mentioned in Section 2.3.1, because of the degeneracy between γ and ζ_{crit} (equation 10), we fix $\gamma = 75$ erg cm^{-2} and vary $\zeta_{\text{crit}} = 2$–30 Å. We here adopt $\zeta_{\text{crit}} = 10$ Å as a fiducial value. Since the grain–grain collision velocities are typically less than 50 m s^{-1} in the dense ISM, we assume for coagulation that the grains always stick when they collide (Wada et al. 2013).

The parameter that regulates the maximum compaction, ϵ_V (equation 14) is also an unknown parameter. As shown later, this parameter basically determines the filling factor of grains larger than submicron. Although this parameter is uncertain, we argue later that $\epsilon_V \lesssim 1$.

If ϵ_V is larger than 1, it imposes an artificial fluffiness for submicron grains as we discuss in Section 3.1. We adopt $\epsilon_V = 0.5$ for the fiducial value but examine the variation of $\epsilon_V = 0$–1 separately.

The number of contact points, n_c, is also unknown since we do not trace each monomer. We interpret this parameter as the number of contacting points whose motion significantly reduces the porosity. We assume $n_c = 30$ unless otherwise stated. We also examine the effect of n_c by changing its value.

2.5.2 Important parameters specific for shattering

In the above, we assumed for shattering that the fragments are compact while the remnant has the same filling factor as the original grain (equation 19). However, compaction could occur for the remnants. Here, for an experimental purpose, we consider a model in which the comparable volume to the ejecta suffers compaction. Noting that the ejecta have a fraction $\varphi/(1+\varphi)$ of the original grain, the compaction of the volume corresponding to that fraction can be written as

$$V_{1+2} = \max\left[\frac{1-\varphi}{1+\varphi}V(m_1) + \frac{\varphi}{1+\varphi}\frac{m_1}{s}, \frac{m_1}{(1+\varphi)s}\right]$$
$$\text{if } m = m_1/(1+\varphi). \quad (24)$$

The first case in the max function describes the replacement of the volume $[\varphi/(1+\varphi)]V(m_1)$ (the original total volume of the ejecta) with $[\varphi/(1+\varphi)]m_1/s$ (the corresponding compact volume). However, this breaks down for large φ, and V_{1+2} could even become negative. Thus, we set the second case in the max function, which describes the fully compact remnant. By default, we use equation (19), but when we include compaction of remnants, we use equation (24) instead of the first condition in equation (19).

2.5.3 Initial condition

Coagulation and shattering basically conserve the total grain mass. Strictly speaking, because we set the upper and lower boundaries for the grain radii ($a_{\text{min}} = 3$ Å and $a_{\text{max}} = 10$ μm, respectively; Section 2.1) and remove all grains coagulated or shattered beyond the boundaries, the total grain mass is not strictly conserved. Except for this effect, our algorithm guarantees the conservation of the total grain mass (see appendix B of Hirashita & Aoyama 2019). We adopt a power-law grain size distribution similar to the MRN distribution: $n_{\text{init}}(a_m) \propto a_m^{-p}$ ($p = 3.5$) with the lower and upper bounds of grain radii being $a_{\text{min,ini}} = 0.001$ μm and $a_{\text{max,ini}} = 0.25$ μm, respectively.[3] This initial grain size distribution is related to the above grain mass distribution as $n_{\text{init}}(a_m) da_m = \tilde{n}(m, t=0) dm$. With the above power-law grain size distribution, we obtain, recalling that $\rho(m,t) = m\tilde{n}(m,t)$,

$$\rho(m, t=0) = \frac{(4-p)\mu_H m_H n_H \mathcal{D}}{3\left[m_{\text{max,ini}}^{(4-p)/3} - m_{\text{min,ini}}^{(4-p)/3}\right]} m^{(-p+1)/3}$$ (25)

for $m_{\text{min,ini}} < m < m_{\text{max,ini}}$, where $m_{\text{max,ini}} = 4\pi a_{\text{max,ini}}^3 s/3$ and $m_{\text{min,ini}} = 4\pi a_{\text{min,ini}}^3 s/3$. We used equation (3) for normalization. Thus, if we give $\mathcal{D}$, we set the initial condition. We adopt $\mathcal{D} = 0.01$

---

[3] Note that $a_{\text{min/max,ini}}$ and $a_{\text{min/max}}$ are different with the latter chosen to be similar to the constraint from MRN. We also confirmed that the results below are insensitive to $a_{\text{min,ini}}$ as long as $a_{\text{min,ini}} \lesssim 0.01$ μm. By the nature of coagulation, grains with $a < a_{\text{min,ini}}$ do not appear in the pure coagulation cases below.

as a typical dust-to-gas ratio in the Milly Way, but remind the reader that the time-scales of coagulation and shattering scale with $\mathcal{D}^{-1}$. The initial filling factor is assumed to be the same (unity unless otherwise stated) for all grains because we do not know the filling factor in advance.

Note that the initial condition here is not meant to represent the initial grain size distribution in a galaxy. It is aimed at setting a 'standard' grain size distribution, based on which we investigate the effect of coagulation and shattering. Therefore, the MRN grain size distribution, which roughly reproduces the dust properties (e.g. extinction curves) in the Milky Way is simply used as a starting point. This initial condition also serves to understand how the extinction curves should be modified by coagulation and shattering. This approach is similar to the one taken by Hirashita & Yan (2009) for compact grains.

3 RESULTS

We show the resulting grain size distributions, filling factors and extinction curves in this section. We first examine coagulation and shattering separately to clarify the effects of each process (these cases are referred to pure coagulation and pure shattering). After that, we clarify the combined effects arising from the ISM phase exchange by including both processes simultaneously (Section 2.5).

In the following, the grain size distribution is always shown in the form of $a_m^4 n(a_m)/n_H$ (the variable t in n is omitted), where the grain size distribution $n(a_m)$ is defined as $n(a_m)\,da_m = \tilde{n}(m)\,dm$ [recall that $m = (4\pi/3)a_m^3 s$]. Since $\rho(m)\,dm = m\tilde{n}(m)\,dm \propto a_m^3 n(a_m)\,da_m \propto a_m^4 n(a_m)\,d\log a_m$, $a_m^4 n(a)$ is proportional to the mass distribution function per $\log a_m$. We further divide this quantity by n_H to cancel out the overall density difference between the dense and diffuse ISM. We refer to $a_m^4 n(a_m)/n_H$ also as the grain size distribution whenever there is no risk of confusion.

3.1 Pure coagulation

We examine the evolution of grain size distribution and filling factor by coagulation in the dense ISM (the pure coagulation case). We show the results in Fig. 1. Coagulation continuously forms large grains, depleting small grains. The bump in the grain size distribution at large grain radii is prominent after coagulation takes place significantly. The height of the bump is almost constant, reflecting the mass conservation in coagulation. Micron-sized grains are formed on a time-scale of 100 Myr, which is consistent with Hirashita & Voshchinnikov (2014, see their figure 4a). Note that this time-scale scales with the assumed density roughly as $\propto n_H^{-3/4}$ as mentioned in Section 2.5 (recall that we adopt $n_H = 10^3$ cm^{-3} for the dense ISM).

We also show the filling factor ϕ_m in Fig. 1. We observe that the filling factor steadily decreases up to $t \sim 100$ Myr because coagulation creates porosity. The decrease of filling factor is governed by coagulation of small grains, which are, however, effectively depleted by coagulation. As the abundance of small grains becomes lower, the decrease of the filling factor is saturated. For large ($a \gtrsim 0.1\ \mu$m) grains, the porosity is determined by the assumption of maximum compaction regulated by ϵ_V in equation (14). The filling factor at large grain radii roughly approaches $\phi_m \sim 1/(1 + \epsilon_V) \simeq 0.67$ (recall that $\epsilon_V = 0.5$). In fact, the value is slightly larger than 0.67, because of our treatment of equation (14): There are still cases where $V_{1,\mathrm{comp}} + V_{2,\mathrm{comp}} < V_{1+2} < (1 + \epsilon_V)(V_{1,\mathrm{comp}} + V_{2,\mathrm{comp}})$. In this case, grains whose filling factors are between $1/(1 + \epsilon_V)$ and 1 form,
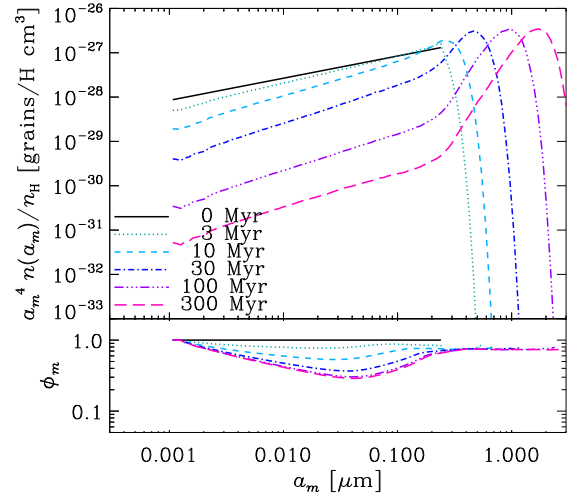
Figure 1. Evolution of grain size distribution (upper window) and filling factor (lower window) for the pure coagulation case. The grain size distribution is multiplied by a_m^4 and divided by n_H, so that the resulting quantity is proportional to the grain mass abundance per $\log a_m$ relative to the gas mass. The solid, dotted, short-dashed, dot–dashed, triple-dot–dashed, and long-dashed lines show the results at $t = 0$ (initial condition), 3, 10, 30, 100, and 300 Myr, respectively. The time evolution of ϕ_m (filling factor) is also shown in the same line species as in the upper window. Note that we use the mass-equivalent grain radius a_m, while the characteristic grain radius is obtained by $a_{\mathrm{ch}} = a_m \phi_m^{-1/3}$.

contributing to raising the averaged ϕ_m above $1/(1 + \epsilon_V)$ at large grain radii.

We also examine the dependence on the parameters relevant for coagulation. First, we present the effect of E_{roll}, which regulates compaction. As indicated in Section 2.3.1, E_{roll} is determined by the critical displacement ξ_{crit} in our model. In Fig. 2a, we show the results for $\xi_{\mathrm{crit}} = 2$, 10, and 30 Å (note that E_{roll} is proportional to ξ_{crit}). We only show the results at $t = 100$ Myr since the effect of ξ_{crit} is qualitatively similar at all ages. We observe that the filling factor at $a \sim 0.1\ \mu$m is affected by the change of ξ_{crit} (or E_{roll}), with larger ξ_{crit} showing smaller ϕ_m. This is because compaction is less efficient in the case of larger ξ_{crit}. In contrast, the filling factor at $a \lesssim 0.01\ \mu$m is not affected by ξ_{crit} because compaction is not important in that grain radius range. The filling factor also converges to the same value determined roughly by $1/(1 + \epsilon_V)$ at the largest grain radii as mentioned above. The grain size distribution, on the other hand, is insensitive to ξ_{crit}. Since the grain abundance is dominated by large grains, small grains collide predominantly with large grains. In this situation, the collisional cross-section is governed by large grains which are almost compact. Thus, the difference in the porosity at submicron radii does not affect the grain size distribution.

Grain compaction is also affected by the number of contacts n_c (equation 12). In Fig. 2b, we show the results for $n_c = 10$, 30, and 100 at $t = 100$ Myr. Naturally, the effect of n_c appears at grain radii where compaction is important. As n_c becomes larger, the filling factor is kept lower against compaction, so that the increase of ϕ_m becomes shallower at large a_m. The grain size distribution is insensitive also to the change of n_c.

We also examine the dependence on ϵ_V, which regulates the maximum compaction. As we argued above, the filling factor roughly converges to $1/(1 + \epsilon_V)$ at large grain radii, where grain velocities are high enough for significant compaction. As shown above, the
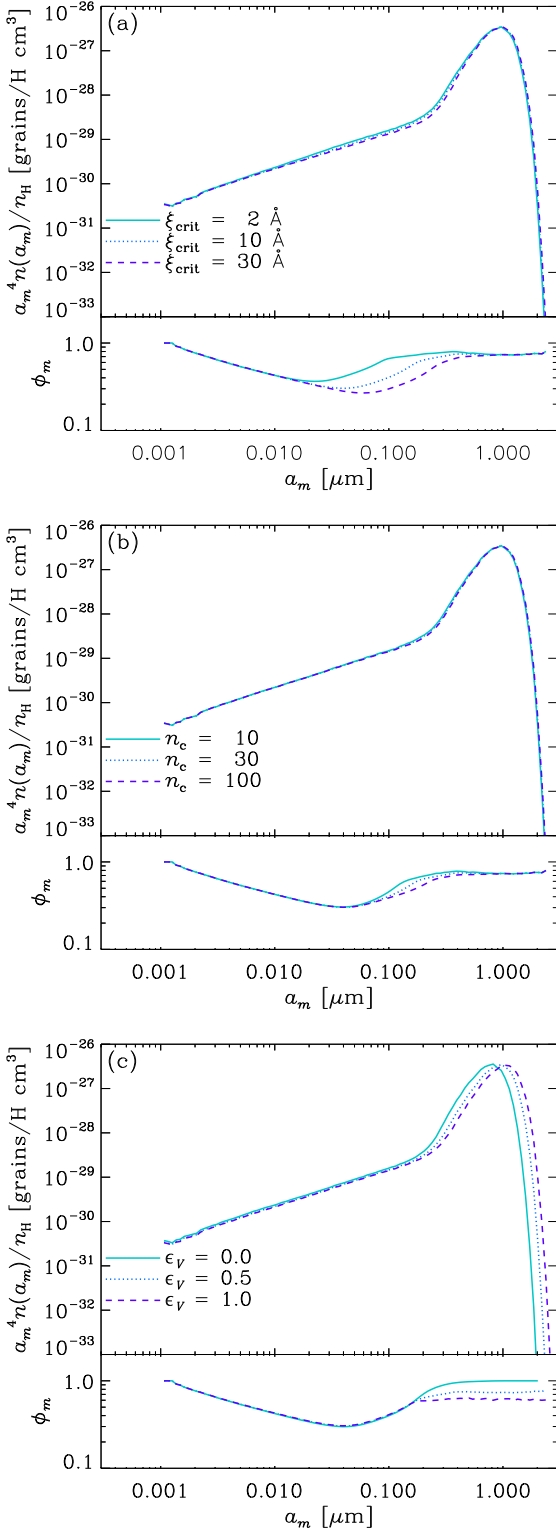
Figure 2. Parameter dependence for the pure coagulation cases. We present the grain size distributions (upper window) and the filling factors (lower window) at $t = 100$ Myr. (a) Dependence on ξ_{crit}, which regulates E_{roll}. The solid, dotted, and dashed lines show the results for $\xi_{crit} = 2$, 10, and 30 Å, respectively. (b) Dependence on n_c, which regulates compaction. The solid, dotted, and dashed lines show the results for $n_c = 10$, 30, and 100, respectively. (c) Dependence on ϵ_V, which regulates the maximum compaction in high-velocity collisions (relevant for large grains). The solid, dotted, and dashed lines show the results for $\epsilon_V = 0$, 0.5, and 1, respectively. Other than the varied parameter in each panel, we adopt the fiducial values ($\xi_{crit} = 10$ Å, $n_c = 30$, and $\epsilon_V = 0.5$).
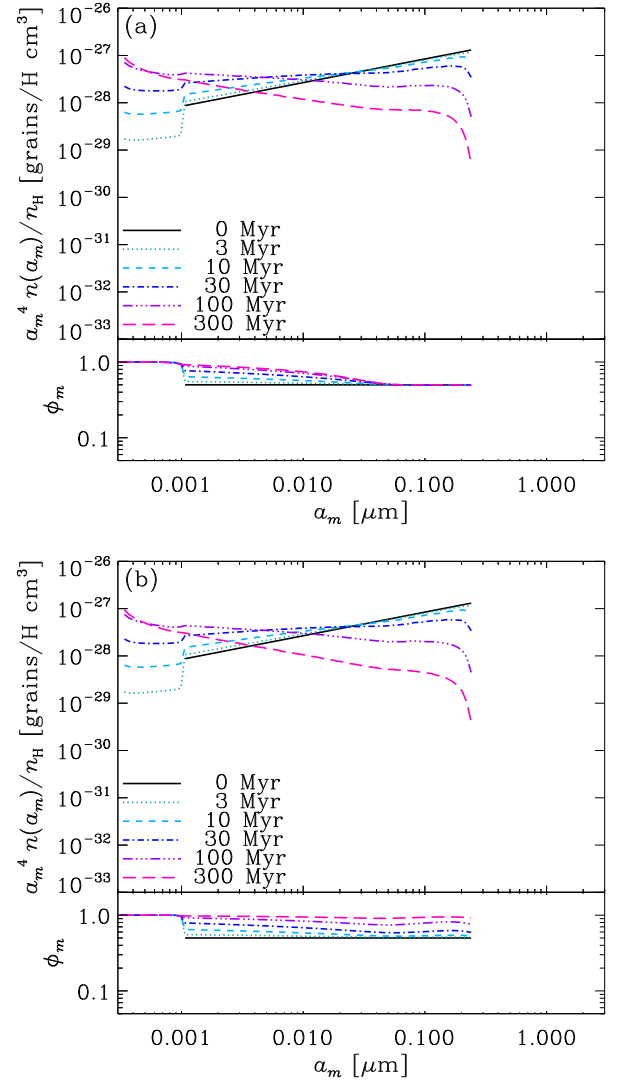
Figure 3. Same as Fig. 1 but for the pure shattering model. We show the cases where we (a) do not consider and (b) consider compaction for the shattered remnants.

minimum value of ϕ_m is around 0.3–0.5. Thus, ϵ_V should be smaller than ~ 1; otherwise, the filling factor at large grain radii decreases below the minimum value, which means that we add artificial (or contradictory) porosity to the grains in compaction. Thus, we examine $\epsilon_V = 0$, 0.5, and 1 at $t = 100$ Myr in Fig. 2c. We confirm that the effect of ϵ_V appears at large grain radii ($a \gtrsim 0.2$ μm). As mentioned above, ϕ_m at large grain radii is roughly $1/(1 + \epsilon_V)$. The grain size distribution is affected by ϵ_V since larger porosity makes the collision kernel larger by a factor of $\phi_m^{-1/3}$ (Section 2.2), which increases the grain–grain collision rate.

3.2 Pure shattering

We show the evolution of grain size distribution and filling factor by shattering in the diffuse ISM. Since shattering does not create new porosity in grains, we start with $\phi_m = 0.5$ for all grains. (If we choose $\phi_m = 1$ as the initial condition, the filling factor is always 1.) We show the results in Fig. 3a. Shattering continuously converts large grains to small grains, creating grains down to the minimum

grain radius $a = 3$ Å. After $t \sim 100$ Myr, the grain abundance is dominated by small grains. The filling factor increases, especially at small grain radii, because shattered fragments are compact. Since we assume that the remnants have the same filling factor as the original grains, the filling factors of the largest grains, which are dominated by shattered remnants, do not change. Recall that the largest fragment size is $(0.02)^{1/3} \simeq 0.27$ times the original grain size (Section 2.3.2). Since the maximum grain radius in the initial condition is 0.25 μm, the largest grain radius where ϕ_m is raised by fragments is $a \simeq 0.27 \times 0.25$ μm $\simeq 0.068$ μm. Thus, the porosity is only changed from its initial value at $a < 0.068$ μm. All the grains with $a < a_{\rm min,ini} = 0.001$ μm are newly formed by shattering; thus, they always have $\phi_m = 1$.

As explained in Section 2.5.2, the shattered remnants could suffer compaction. In order to examine this effect, we also show the case with compaction of remnants; that is, we adopt equation (24) instead of the first condition in equation (19) for the remnant volume. In Fig. 3b, we show the evolution of grain size distribution and filling factor with including remnant compaction. The grain size distributions are little affected by the treatment of the remnant volume, while the filling factor at large grain radii increases if we take compaction of remnants into account. Because shattering never creates porosity, the filling factors of all grains converge to unity on a time-scale of depleting large grains by shattering (100–300 Myr).
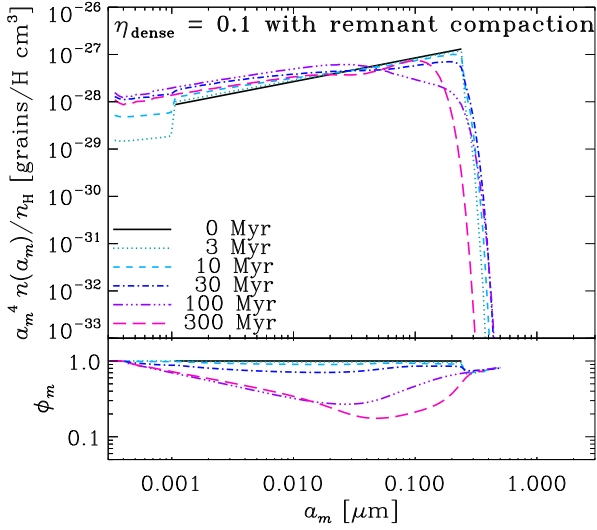
3.3 Coagulation and shattering

If we consider the grain size distribution in a region large enough to include both the dense and diffuse ISM (or if we consider time-scales much longer than the phase-exchange time; Section 2.5), the effect of coagulation and that of shattering coexist. In our one-zone model, we could simulate this coexisting effect by simultaneously treating coagulation and shattering at each time-step with a weight of $\eta_{\rm dense} : (1 - \eta_{\rm dense})$ as formulated in equations (22) and (23). We adopt $\eta_{\rm dense} = 0.5$ first as a fiducial value (that is, the grains spend half of their times in the dense ISM). In Fig. 4a, we show the evolution of grain size distribution and filling factor.

We observe in Fig. 4a that, if both coagulation and shattering are present, the grain size distribution maintains a power-law-like shape. It is also interesting to note that the slope is similar to that of the MRN distribution. It has been shown that the slope of grain size distribution converges to a value similar to the MRN distribution if efficient fragmentation and/or coagulation occur (e.g. Dohnanyi 1969; Williams & Wetherill 1994; Tanaka et al. 1996; Kobayashi & Tanaka 2010). Coagulation is slightly 'stronger' than shattering, so that large (submicron) grains gradually increase. The grain size distribution and filling factor reach an equilibrium around $t \sim 100$ Myr. The filling factor changes in a way similar to the pure coagulation case (Fig. 1) but the decrease of the filling factor proceeds more if both coagulation and shattering are present because small grains which coagulate to form porosity are continuously supplied. The filling factor at large grain radii converges to $\sim 1/(1 + \epsilon_V)$ as explained in Section 3.1.

To examine the balance between coagulation and shattering, we also show the results for different values of $\eta_{\rm dense}$ (0.1 and 0.9) in Fig. 4. Naturally, a higher abundance of large grains is obtained for larger $\eta_{\rm dense}$. For $\eta_{\rm dense} = 0.9$, the result is similar to that in the pure coagulation case (Fig. 1), except that small grains continue to be produced by shattering. The case of $\eta_{\rm dense} = 0.1$ has the following two interesting properties: (i) The evolution of grain size distribution is not monotonic. Indeed, large grains are continuously converted into small grains up to $t \sim 100$ Myr but large grains increase ('re-form')
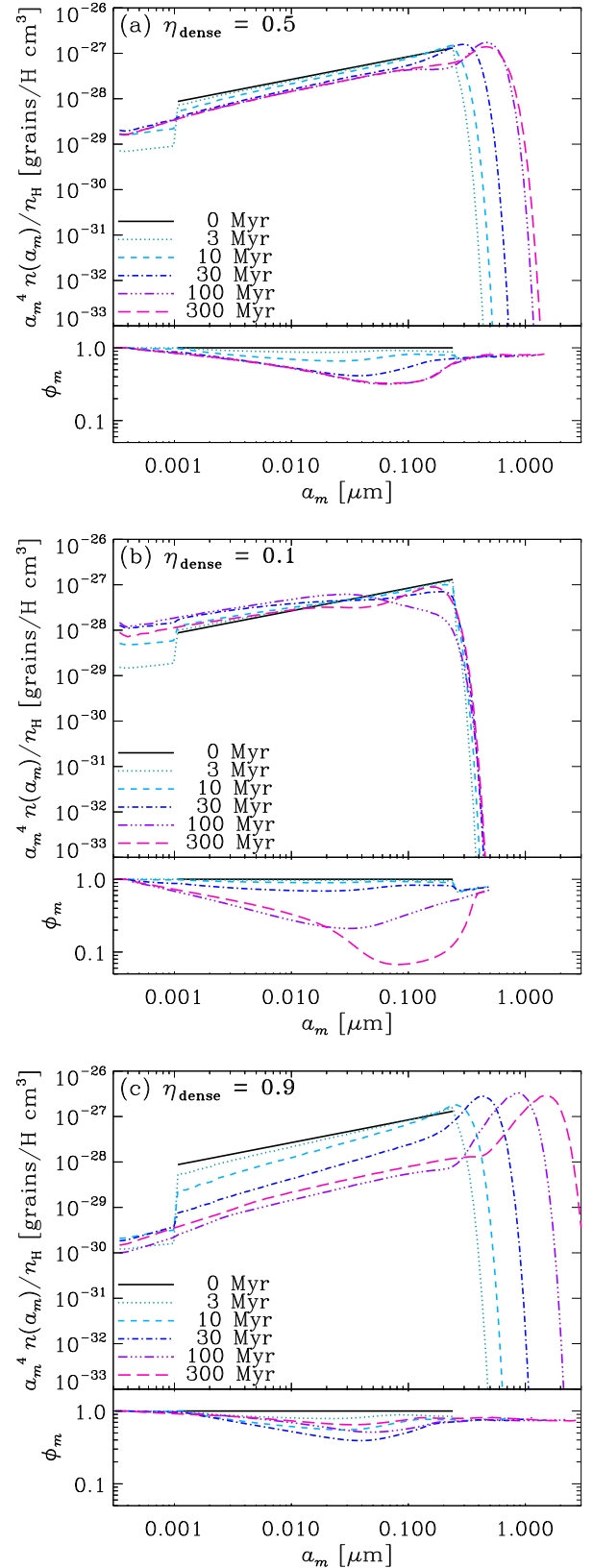
Figure 4. Same as in Fig. 1, but including both shattering and coagulation. Panels (a), (b) and (c) show the results for $\eta_{\rm dense} = 0.5$ (fiducial), 0.1, and 0.9, respectively. Note the different scale of ϕ_m between this figure and Fig. 1.

Figure 5. Same as Fig. 4b but with compaction of shattered remnants.

after that. (ii) The filling factor becomes very small at $t > 100$ Myr. This is because the production of small grains by shattering continuously activates coagulation, which creates porosity. The increased porosity makes the geometrical cross-section larger, and enhances coagulation. Moreover, since the velocities of porous grains are reduced, compaction does not occur as efficiently as in the pure coagulation case. Thus, efficient shattering together with coagulation makes the interstellar dust highly porous and further activates coagulation. This interesting interplay is further discussed in Section 5.

The dependences on the parameters related to coagulation (ξ_{crit}, n_c and ϵ_V) are similar to those shown in Section 3.1 (Fig. 2). On the other hand, compaction of shattered remnants (Section 2.5.2) could decrease the porosity if η_{dense} is low. In Fig. 5, we show the results with compaction of shattered remnants for $\eta_{dense} = 0.1$. This figure should be compared with Fig. 4b. We observe that the filling factor becomes higher at $t \sim 300$ Myr at large grain radii, although the results are almost unchanged at younger ages. Compaction of remnants also makes coagulation at later epochs less efficient, producing less large grains at $t \sim 300$ Myr. However, the filling factor is still as small as 0.1–0.2 at $a \sim 0.1$ μm at $t \sim 300$ Myr; thus, the conclusion that efficient shattering together with coagulation helps to increase porosity is robust.

4 EXTINCTION CURVES

Based on the grain size distributions and the filling factors presented above, we calculate the extinction curves by the method in Section 2.4 for silicate and amC. As mentioned above, the extinction A_λ is presented in two ways: A_λ/N_H and A_λ/A_V. To clarify the effect of porosity, we also calculate extinction curve by forcing the filling factor of all grains to be unity with a_m fixed. The extinction calculated in this way (i.e. $\phi_m = 1$) is denoted as $A_{\lambda,1}$. The effect of porosity is presented by $A_\lambda/A_{\lambda,1}$.

4.1 Effect of coagulation

In Fig. 6, we present the extinction curves corresponding to the grain size distributions and the filling factors for the pure coagulation case
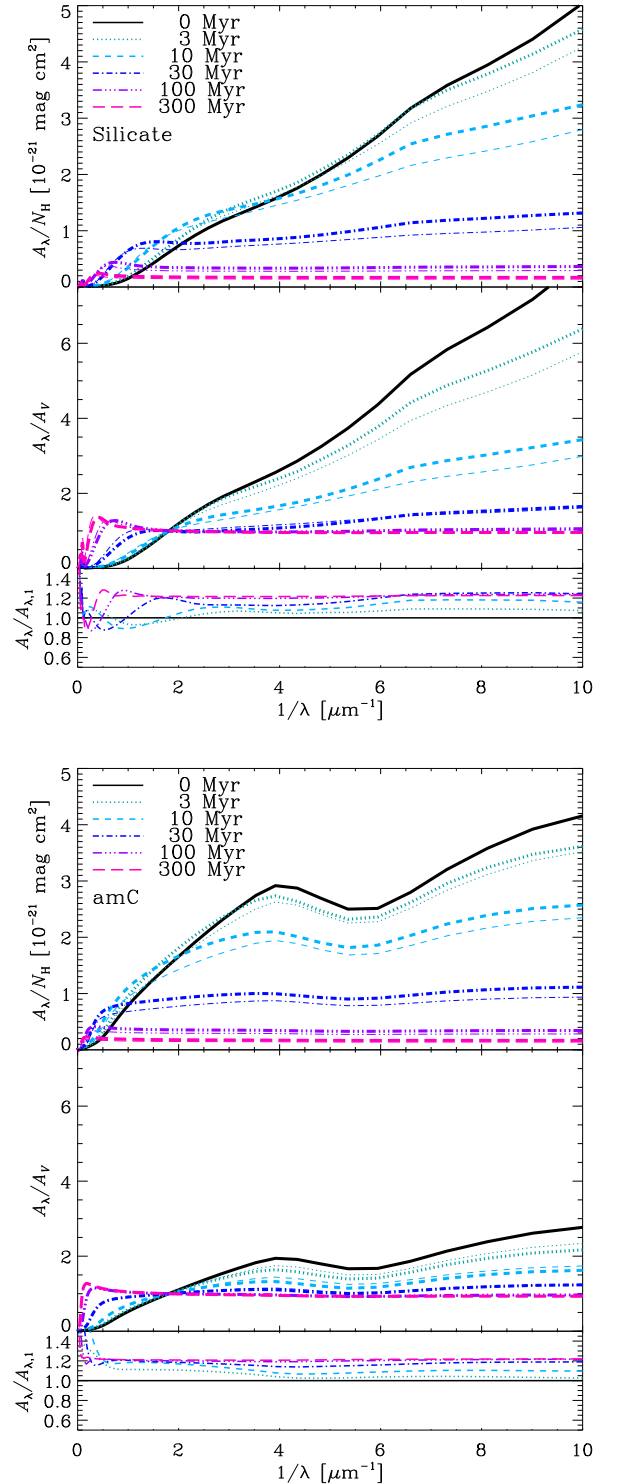
Figure 6. Extinction curves for silicate and amC in the upper and lower panels, respectively. The solid, dotted, short-dashed, dot–dashed, triple-dot–dashed, and long-dashed lines (thick lines) show the extinction curves at $t = 0$ (initial condition), 3, 10, 30, 100, and 300 Myr, respectively. The thin lines with the same line species show $A_{\lambda,1}$ (extinction with $\phi_m = 1$). Note that $A_\lambda = A_{\lambda,1}$ at $t = 0$. In each panel, the upper, middle, and lower windows present the extinction per hydrogen, the extinction normalized to the V-band value, and the ratio of A_λ to $A_{\lambda,1}$ (an indicator of the porosity effect), respectively.

(Fig. 1). As expected from the evolution of grain size distribution, the extinction curve becomes flatter as coagulation proceeds. Since a large fraction of the grains become bigger than $\sim 0.1\ \mu$m after coagulation, the extinction per hydrogen declines at wavelengths shorter than $\sim 2\pi \times 0.1\ \mu$m for both materials. The effect of porosity, which appears in the difference between A_λ (thick lines) and $A_{\lambda,1}$ (thin lines) or in the ratio $A_\lambda/A_{\lambda,1}$ shown in the bottom window, is clear. The extinction is 10–20 per cent higher in the porous case than in the non-porous case in a large part of wavelengths for both materials.

There are some differences between the two materials. For silicate, porous grains have smaller extinction than compact ones in a certain wavelength range (e.g. $1/\lambda \sim 0.5$–$2\ \mu$m^{-1} at $t = 10$ Myr) and this range shifts to longer wavelengths with age. Voshchinnikov et al. (2006) and Shen et al. (2008) showed that the porosity could both increase and decrease the extinction cross-section depending on the wavelength. The wavelength range of suppressed extinction by porosity is roughly consistent with their results. Voshchinnikov et al. (2006) also showed that the wavelength range where the extinction cross-section is decreased by porosity shifts to longer wavelengths as the grains become larger. This is consistent with our result. At $t \lesssim 100$ Myr, the normalized extinction curves (A_λ/A_V) becomes steeper by the porosity because the increase of extinction is more enhanced in the UV than in the V band.

For amC, porosity always increases the extinction; that is, $A_\lambda/A_{\lambda,1}$ is always larger than 1. Thus, if we normalize the extinction to A_V, the porosity effect roughly cancels out, so that the extinction curve shape is insensitive to the porosity (filling factor) for amC.

We also examined the parameter dependence (not shown) and confirmed that the extinction curves are not sensitive to $\xi_{\rm crit}$ or ϵ_V in the optical and UV with differences less than 5 per cent. However, at $1/\lambda < 2\ \mu$m^{-1}, the difference could be as large as 20 per cent, since, at such long wavelengths, the porosity of large grains, which is regulated by $\xi_{\rm crit}$ and ϵ_V, is important. The changes driven by the difference in parameters are sub-dominant compared with those parameters are sub-dominant compared with the difference between porous and non-porous grains shown in Fig. 6.

4.2 Inclusion of shattering

In the pure shattering case, the filling factor simply tends to increase; thus, the resulting extinction curve approaches the one with compact grains. More important is the interplay between shattering and coagulation as shown above. Indeed, coagulation of newly created small grains by shattering produces porous grains, contributing to the increase of porosity in the interstellar dust. Here, we investigate the effect of relative strength between shattering and coagulation; that is, we compare the results for different dense gas fractions, $\eta_{\rm dense}$.

In Fig. 7, we compare the extinction curves calculated for the models including both coagulation and shattering. The corresponding grain size distributions are shown in Section 3.3 (Fig. 4). We compare the results at the same age $t = 100$ Myr. We observe that the steepness of extinction curve is very sensitive to $\eta_{\rm dense}$. This is a natural consequence of the different grain size distributions for various $\eta_{\rm dense}$. We also plot the extinction curves with $\phi_m = 1$ (with the same distribution of a_m), that is, $A_{\lambda,1}$. Comparing A_λ with $A_{\lambda,1}$, we observe for silicate that the porosity increases the extinction at short and long wavelengths, but that it rather decreases the extinction at intermediate wavelengths as already noted in the previous subsection. The wavelength range where the porosity decreases the extinction shifts to shorter wavelengths for smaller $\eta_{\rm dense}$, which is consistent with the above mentioned tendency that porosity of smaller grains reduces the extinction at shorter wavelengths. For amC, the
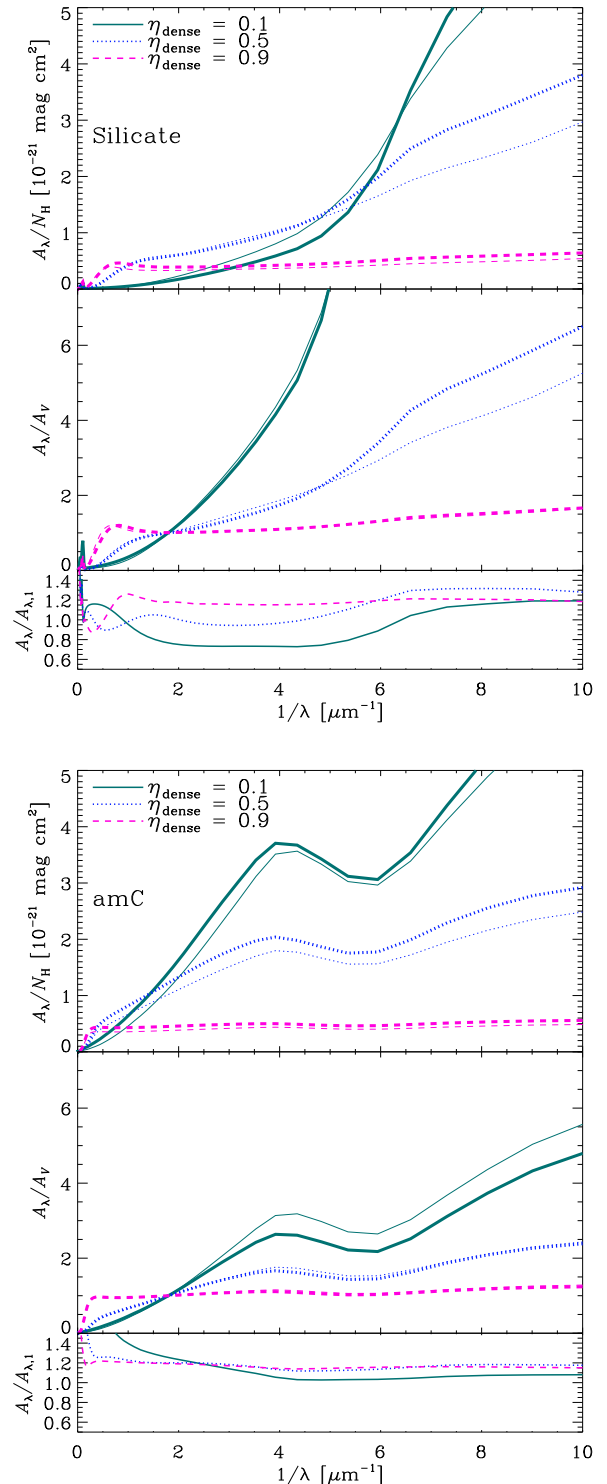
Figure 7. Comparison among the extinction curves in the models including both coagulation and shattering. The relative strengths of these two processes are regulated by the dense gas fraction $\eta_{\rm dense}$. We show the same quantities as in Fig. 6 at $t = 100$ Myr. The solid, dotted, and dashed lines show the results for $\eta_{\rm dense} = 0.1$, 0.5, and 0.9, respectively. The thick and thin lines present the cases using the calculated filling factors (Fig. 4) and those with $\phi_m = 1$ (the filling factor is forced to be unity; i.e. $A_{\lambda,1}$). The upper and lower panels are for silicate and amC, respectively.

porosity always increases the extinction, but the largest porosity (i.e. $\eta_{\text{dense}} = 0.1$) does not necessarily mean the largest opacity enhancement ($A_\lambda/A_{\lambda,1}$) in the UV. At long wavelengths, larger porosity indicates larger extinction.

Overall, the effect of porosity on the extinction curve is less than 20 per cent as far as the UV–optical extinction curves are concerned, but this could mean that we 'save' up to 20 per cent of metals to realize an observed extinction if we take porosity into account. The difference is not large, though, because the increase of grain volume and the 'dilution' of permittivity have opposite effects on the extinction (Li 2005). For further constraint on the porosity evolution, we need a comprehensive analysis of observed dust properties including the infrared SED (Dwek et al. 1997). Polarization may also help to further constrain the models. Since such a detailed comparison also needs further modelling of the mixture of various dust species and of the interstellar radiation field, we leave it for a future work.

5 DISCUSSION

5.1 Effects of porosity on the evolution of grain size distribution

The porosity increases the effective sizes of grains, enhancing the grain–grain collision rate. If only coagulation occurs, however, the porosity, which is large at $a \lesssim 0.1\ \mu$m, does not have a large influence on the grain size distribution, since grains quickly coagulate to achieve $a \gtrsim 0.1\ \mu$m, and are affected by compaction. Note that, if we individually observe clouds denser than $n_{\text{H}} \sim 10^3\ \text{cm}^{-3}$, we could find very fluffy grains as will be shown by L. Pagani et al. (in preparation) (see also Hirashita & Li 2013; Wong et al. 2016). The major part of interstellar grains are smaller than 1 μm (e.g. Weingartner & Draine 2001b), so that the grains in such dense clouds are not likely to contribute directly to the interstellar dust population.

Coagulation can be balanced by shattering. For $\eta_{\text{cold}} = 0.5$, the grain size distribution and the filling factor both converge to equilibrium distributions at $t \sim 100$ Myr, while coagulation continuously increases the grain radii for $\eta_{\text{cold}} = 0.9$ (Section 3.3; Fig. 4). Thus, cases with high η_{cold} produce similar results to the pure coagulation case. For the case of $\eta_{\text{cold}} = 0.5$, we performed a calculation by forcing ϕ_m to be always unity (not shown) and found that the grain size distribution changes little by the different treatment of ϕ_m (i.e. compared with the results shown in Fig. 4a). This is because the evolution of grain size distribution is regulated by the formation of large grains (recall that the grain abundance is dominated by large grains), which have small porosity because of compaction.

Porosity plays a critical role in the case of small $\eta_{\text{dense}} = 0.1$. As discussed in Section 3.3 (Fig. 5), the grain size distribution is first dominated by shattering, which decreases the abundance of large grains, while coagulation gradually recovers the large-grain abundance at later stages (typically after $t \sim 100$ Myr). We argued above that coagulation is activated at $t \sim 100$ Myr because the increased porosity enhances the grain cross-sections (the grain–grain collision rate). For demonstration, we compare two calculations in Fig. 8: one is the same as above for $\eta_{\text{dense}} = 0.1$ (Fig. 4b), and the other is a calculation with the same setting but with $\phi_m = 1$ (i.e. without porosity). Since the difference is not prominent on a short time-scale, we focus on the evolution after $t = 100$ Myr. If we fix $\phi_m = 1$, grains at $a \gtrsim 0.1\ \mu$m are simply depleted by shattering as expected from weak coagulation in $\eta_{\text{dense}} = 0.1$. In contrast, if we take the evolution of ϕ_m into account, grains at $a \gtrsim 0.1\ \mu$m are re-formed at $t \gtrsim 200$ Myr, reaching roughly an equilibrium at $t \sim 400$ Myr. The filling factor reaches the smallest value ($\phi_m \sim 0.1$)
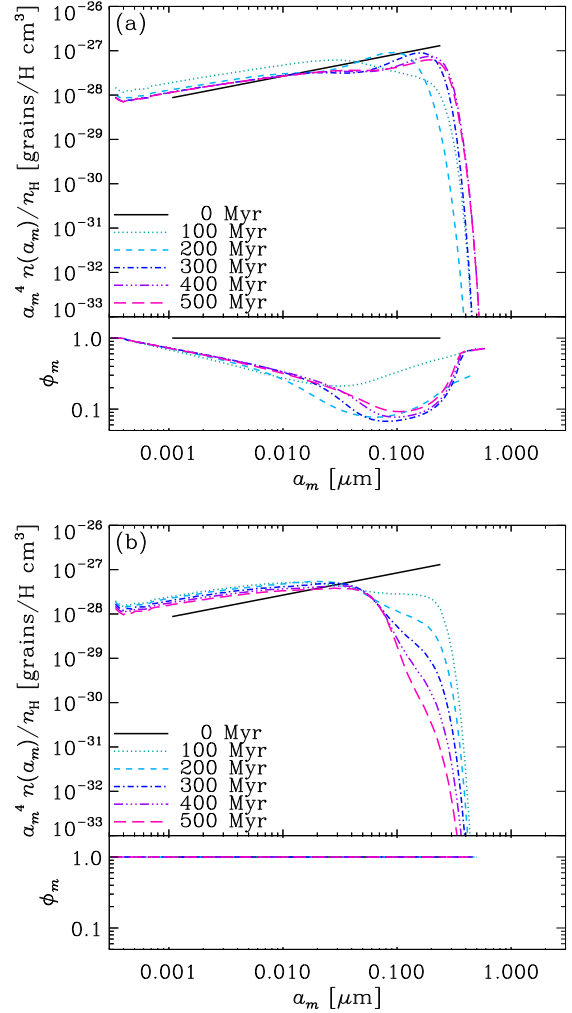
Figure 8. Long-term evolution of grain size distribution and filling factor with both coagulation and shattering under $\eta_{\text{dense}} = 0.1$. Panels (a) and (b) show the results with including the evolution of filling factor (i.e. the same model as in Fig. 4b) and with fixing $\phi_m = 1$, respectively. We present the results at $t = 0$, 100, 200, 300, 400, and 500 Myr (at $t < 100$ Myr, the two results have little difference) by the solid, dotted, short-dashed, dot–dashed, triple-dot–dashed, and long-dashed lines, respectively.

at $a \sim 0.1\ \mu$m. There are two effects that promote coagulation at later stages: (i) The increase of grain cross-sections by porosity enhances the grain–grain collision rate because the collision kernel scales with the porosity as $\propto \phi_m^{-1/3}$ (Section 2.2). (ii) The decreased grain velocity ($\propto \phi_m^{1/3}$; equation 6) makes compaction in coagulation at large grain radii less effective, so that the filling factor is kept small even at $a \sim 0.1\ \mu$m. These two effects are persistent qualitatively even if we consider the compaction of shattered remnants (see Fig. 5).

Recall that our treatment of the two-phase ISM is based on the parameter η_{dense}, which sets the fraction of time dust spends in the dense phase. Thus, the above results imply that the dust evolution in a condition where both coagulation and shattering coexist (in a wide area of the ISM and/or on a time-scale longer than the phase exchange time-scale $\sim 10^7$ yr; Section 2.5) could be strongly affected by porosity. In other words, dust evolution models which do not include porosity evolution could predict a very different evolution

of the grain size distribution from those which correctly take the porosity evolution into account.

For a long-term evolution of dust in the ISM, dust enrichment by stellar ejecta, dust growth by the accretion of gas-phase metals, and dust destruction by supernova shocks are also important (e.g. Dwek 1998). Thus, it is interesting to additionally model the porosity evolution in these processes. This paper provides a first important step for the understanding of porosity evolution since coagulation and shattering are mechanisms of efficiently modifying the grain size distribution. Indeed, Hirashita & Aoyama (2019) emphasized the importance of these two processes in realizing MRN-like grain size distributions (see also Aoyama et al. 2020).

5.2 Effects of porosity on extinction curves

As shown in Section 4, porosity affects the UV–optical extinction curves by 10–20 per cent. As noted by Voshchinnikov et al. (2006), porosity does not necessarily increase the extinction (see also Jones 1988; Li 2005). At long-optical and near infrared wavelengths, the opacity of silicate can decrease owing to the porosity. The wavelength range where this decrease occurs shifts towards shorter wavelengths as the typical grain radius becomes smaller in e.g. a shattering-dominated condition. The extinction of amC is enhanced by 10–20 per cent at all wavelengths. The above results indicate that we could save 10–20 per cent of dust to explain the opacity, especially at long (far-infrared) and short (UV) wavelengths.

The effects of porosity on extinction curves are further pronounced given that the evolution of grain size distribution is affected by the filling factor. As shown above, porosity has the largest effect on the grain size distribution if strong shattering and weak coagulation are both present such as in the case of $\eta_{\mathrm{dense}} = 0.1$. Thus, the extinction curve is affected by porosity not only through the optical properties but also through the modification of grain size distribution. To present this effect, we show in Fig. 9 the extinction curves corresponding to the cases shown in Fig. 8. On such a long time-scale as shown in Fig. 8, the loss of dust through the lower grain radius boundary by shattering (recall that we remove the grains which become smaller than $a = 3$ Å) leads to a decrease of $A_\lambda / N_{\mathrm{H}}$ just because of the boundary condition. Thus, we only show A_λ / A_V, which is free from the effect of dust mass loss (i.e. we could purely observe the effect of grain size distribution). For the case without porosity evolution ($\phi_m = 1$), the extinction curve continues to be steepened because shattering continues to convert large grains to small grains. If the porosity evolution is included, the extinction curve is flattened with age because large grains are 'recreated' by enhanced coagulation at later times. Both species show steeper extinction curves than the initial state for the case with porosity evolution although the grain size distributions are similar to the initial condition (Fig. 8). This is because the grain opacity does not increase in the V band, where the extinction curve is normalized, while porosity enhances the UV extinction by 30–40 per cent. Jones (1988) and Voshchinnikov et al. (2006) also showed that porosity does not change the optical extinction much but increase the UV and infrared opacities. This effect makes the UV extinction curve normalized to the V-band value steep.

The case shown in Figs. 8 and 9 indicates that porosity evolution can have a dramatic impact on the shape of extinction curves. Even if the grain size distribution becomes the one similar to the initial grain size distribution at later stages of evolution, the small porosity makes the extinction curves significantly steeper than the initial one. In particular, the grains contributing to the optical extinction have radii $a \sim \lambda/(2\pi) \sim 0.1$ μm, where the porosity is the largest. Therefore, if we consider the creation of porosity through the interplay between
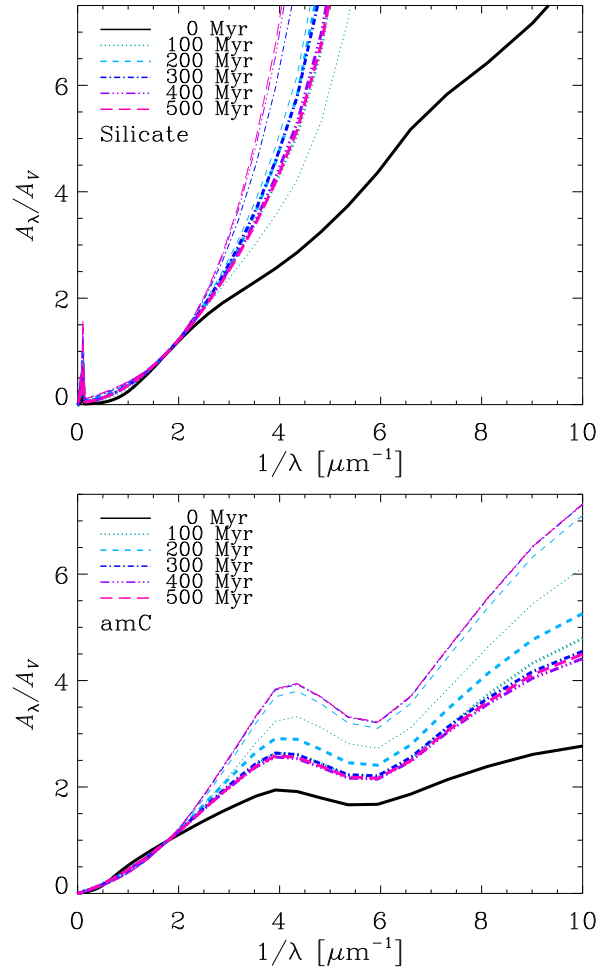
Figure 9. Evolution of extinction curve for the model with $\eta_{\mathrm{dense}} = 0.1$ shown in Fig. 8. Upper and lower panels present the results for silicate and amC, respectively. The correspondence between the line species and the age is the same as in Fig. 8. The thick and thin lines show the results with the evolution of porosity (Fig. 8a) and with forcing ϕ_m to be always unity (Fig. 8b). Note that $\phi_m = 1$ at $t = 0$ for both cases.

coagulation and shattering, the evolution of extinction curve could be qualitatively very different. Moreover, the porosity depends on the grain radius; this dependence also creates 'higher-order' wavelength dependence of extinction curve. As shown above, the wavelength range where the extinction is reduced by porosity shifts to longer wavelengths if porosity is developed in larger grains.

As shown in Section 3.3 (Fig. 5), if we consider compaction of shattered remnants, the filling factor increases a little at $t \gtrsim 300$ Myr. We also calculated the evolution of extinction curve with remnant compaction (now shown). Since coagulation is less efficient in this case, the extinction curves are steeper than those shown in Fig. 9. If we only see the extinction curve shape in the UV–optical, a larger filling factor and a lower abundance of large grains are degenerate.

6 CONCLUSION

We formulate and calculate the evolution of grain size distribution and filling factor (porosity) through coagulation and shattering in the ISM. We adopt the 2D Smoluchowski equation to solve the distribu-

tion functions of grain size and filling factor. To save the computational time, we only treat the mean filling factor for each grain radius based on O09 and O12. For coagulation, the transition from the hit-and-stick to compaction regime are characterized and modelled by comparing the impact energy with the rolling energy. Shattering is treated as a formation mechanism of small compact fragments. For shattered remnants, we basically assume the same porosity as the original grain but we also examine the case where the volume equal to the colliding particle suffers perfect compaction. We assume that coagulation and shattering are hosted by the dense and diffuse ISM, respectively.

For the pure coagulation case (without shattering), the porosity develops around $a \sim 0.01$–0.1 μm, where a low filling factor of $\phi_m \sim 0.3$ is achieved. However, when the porosity becomes significantly large, the major part of grains have already been coagulated to $a > 0.1$ μm, where compaction occurs. Therefore, the porosity little affects the evolution of grain size distribution if only coagulation is present. For the pure shattering case, we confirm that shattering tends to make the filling factors asymptotically approach $\phi_m = 1$ at $a \lesssim 0.01$ μm, although those at $a \gtrsim 0.03$ μm depend on the treatment of compaction for shattered remnants.

Next, we examine the case where coagulation and shattering are both present. This corresponds to a situation where we consider a wide enough area in the ISM which contains both the dense and diffuse ISM, or where the time-scale of interest is much longer than the exchange time of the ISM phases. We find that the filling factor drops even below 0.1 around $a \sim 0.1$ μm. The porosity evolution is sensitive to the relative efficiency of coagulation to shattering, which is regulated by the dense gas fraction, $\eta_{\rm dense}$. The filling factor tends to be small if shattering is stronger (e.g. $\eta_{\rm dense} = 0.1$). This is because shattering continues to efficiently provide small grains, which are subsequently coagulated to form porous grains. Thus, the interplay between shattering and coagulation is fundamentally important as an origin of the porosity in the interstellar grains. For the case with $\eta_{\rm dense} = 0.1$, coagulation is activated in later stages (after porosity develops) because the high porosity enhances the grain cross-sections. Compaction is not efficient in this case since the grain velocity is diminished by the increased porosity. Thus, large grains are kept porous in this case.

We also calculate the evolution of extinction curve using the EMT. Porosity formed as a result of coagulation enhances the UV and infrared extinction by $\sim$10–20 per cent. As noted in previous studies, the extinction of porous silicate grains is suppressed in the optical, and the wavelength range where the extinction is suppressed shifts towards shorter wavelengths if small grains are more abundant (or shattering is more efficient). The extinction is enhanced at all wavelengths for amC in most of the cases. A case with strong shattering ($\eta_{\rm dense} = 0.1$) shows a recreation of large grains at later stages as mentioned above. In this case, although the grain size distribution itself is similar to the MRN distribution, the extinction curve shape stays steep if we normalize the extinction to the V band value. This is because porosity makes the grains relatively 'transparent' in the optical, while the extinction is enhanced in the UV. Thus, the steepness of extinction curve is also affected by the porosity evolution.

Although the predicted features in the extinction curves could be compared with observations, our model developed in this paper is still premature for detailed comparison. There are two necessary extensions of our modelling. First, we could include other processes which also play an important role in the evolution of grain size distribution; that is, dust production by stellar ejecta, dust destruction by supernova shocks, and dust growth by the accretion of gas-phase metals. Secondly, since the filling factor and the grain size distri-

bution could be degenerate in the resulting extinction curve shape, it is desirable to predict other independent properties such as infrared emission SED and polarization. We emphasize that the basic framework developed in this paper provides a basis on which we will extend our predictions.

DATA AVAILABILITY

The data underlying this article are available in Figshare at https://doi.org/10.6084/m9.figshare.12917375.v1.

REFERENCES

Aoyama S., Hirashita H., Nagamine K., 2020, MNRAS, 491, 3844
Asano R. S., Takeuchi T. T., Hirashita H., Nozawa T., 2013, MNRAS, 432, 637
Asano R. S., Takeuchi T. T., Hirashita H., Nozawa T., 2014, MNRAS, 440, 134
Bohren C. F., Huffman D. R., 1983, Absorption and Scattering of Light by Small Particles. Wiley, New York
Cazaux S., Tielens A. G. G. M., 2004, ApJ, 604, 222
Chen L.-H., Hirashita H., Hou K.-C., Aoyama S., Shimizu I., Nagamine K., 2018, MNRAS, 474, 1545
Désert F. X., Boulanger F., Puget J. L., 1990, A&A, 500, 313
Dohnanyi J. S., 1969, J. Geophys. Res., 74, 2531
Dominik C., Tielens A. G. G. M., 1997, ApJ, 480, 647
Draine B. T., 1990, in Blitz L., ed., Astronomical Society of the Pacific Conference Series Vol. 12, The Evolution of the Interstellar Medium. Astron. Soc. Pac., San Francisco, pp 193–205
Draine B. T., 2003, ApJ, 598, 1026
Draine B. T., 2009, in Henning T., Grün E., Steinacker J., eds, Astronomical Society of the Pacific Conference Series Vol. 414, Cosmic Dust - Near and Far. Astron. Soc. Pac., San Francisco, p. 453
Draine B. T., Hensley B. S., 2020, ApJ, submitted, arXiv:2009.11314
Draine B. T., Tan J. C., 2003, ApJ, 594, 347
Dwek E., 1998, ApJ, 501, 643
Dwek E., et al., 1997, ApJ, 475, 565
Gould R. J., Salpeter E. E., 1963, ApJ, 138, 393
Guillet V., Pineau Des Forêts G., Jones A. P., 2011, A&A, 527, A123
Guillet V., Hennebelle P., Pineau des Forêts G., Marcowith A., Commerçon B., Marchand P., 2020, A&A, 643, A17
Heim L.-O., Blum J., Preuss M., Butt H.-J., 1999, Phys. Rev. Lett., 83, 3328
Hensley B. S., Draine B. T., 2020, ApJ, submitted, arXiv:2009.00018
Hirashita H., 1999, ApJ, 510, L99
Hirashita H., Aoyama S., 2019, MNRAS, 482, 2555
Hirashita H., Kobayashi H., 2013, Earth, Planets, and Space, 65, 1083
Hirashita H., Li Z.-Y., 2013, MNRAS, 434, L70
Hirashita H., Voshchinnikov N. V., 2014, MNRAS, 437, 1636
Hirashita H., Yan H., 2009, MNRAS, 394, 1061
Hoang T., 2019, ApJ, 876, 13

Inoue A. K., 2011, Earth, Planets, and Space, 63, 1027

Israelachvili J., 1992, Intermolecular and Surface Forces, 2nd edn. Academic Press, London

Jones A. P., 1988, MNRAS, 234, 209

Jones A. P., Tielens A. G. G. M., Hollenbach D. J., McKee C. F., 1994, ApJ, 433, 797

Jones A. P., Tielens A. G. G. M., Hollenbach D. J., 1996, ApJ, 469, 740

Jones A. P., Köhler M., Ysard N., Bocchio M., Verstraete L., 2017, A&A, 602, A46

Kataoka A., Okuzumi S., Tanaka H., Nomura H., 2014, A&A, 568, A42

Kimura H., Wada K., Senshu H., Kobayashi H., 2015, ApJ, 812, 67

Kobayashi H., Tanaka H., 2010, Icarus, 206, 735

Kusaka T., Nakano T., Hayashi C., 1970, Progress of Theoretical Physics, 44, 1580

Lefèvre C., Pagani L., Ladjelate B., Min M., Hirashita H., Zylka R., 2020, in Mayet F., Catalano A., Macías-Pérez J., Perotto L., eds, European Physical Journal Web of Conferences Vol. 228, European Physical Journal Web of Conferences. Grenoble, p. 00013

Li A., 2005, ApJ, 622, 965

Li A., Draine B. T., 2001, ApJ, 554, 778

Li A., Greenberg J. M., 1997, A&A, 323, 566

Li A., Lunine J. I., 2003, ApJ, 590, 368

Lisenfeld U., Ferrara A., 1998, ApJ, 496, 145

Mathis J. S., 1996, ApJ, 472, 643

Mathis J. S., Whiffen G., 1989, ApJ, 341, 808

Mathis J. S., Rumpl W., Nordsieck K. H., 1977, ApJ, 217, 425

Mathis J. S., Cohen D., Finley J. P., Krautter J., 1995, ApJ, 449, 320

Mattsson L., 2016, Planet. Space Sci., 133, 107

Mattsson L., De Cia A., Andersen A. C., Zafar T., 2014, MNRAS, 440, 1562

McKee C., 1989, in Allamandola L. J., Tielens A. G. G. M., eds, IAU Symposium Vol. 135, Interstellar Dust. Kluwer Academic Publishers, Dordrecht, p. 431

O'Donnell J. E., Mathis J. S., 1997, ApJ, 479, 806

Okuzumi S., Tanaka H., Sakagami M.-a., 2009, ApJ, 707, 1247

Okuzumi S., Tanaka H., Kobayashi H., Wada K., 2012, ApJ, 752, 106

Ormel C. W., Spaans M., Tielens A. G. G. M., 2007, A&A, 461, 215

Ormel C. W., Paszun D., Dominik C., Tielens A. G. G. M., 2009, A&A, 502, 845

Ormel C. W., Min M., Tielens A. G. G. M., Dominik C., Paszun D., 2011, A&A, 532, A43

Rouillé G., Jäger C., Krasnokutski S. A., Krebsz M., Henning T., 2014, Faraday Discuss., 168, 449

Rouillé G., Jäger C., Henning T., 2020, ApJ, 892, 96

Shen Y., Draine B. T., Johnson E. T., 2008, ApJ, 689, 260

Silsbee K., Ivlev A. V., Sipilä O., Caselli P., Zhao B., 2020, A&A, 641, A39

Smith R. K., Dwek E., 1998, ApJ, 503, 831

Steinpilz T., Teiser J., Wurm G., 2019, ApJ, 874, 60

Suyama T., Wada K., Tanaka H., Okuzumi S., 2012, ApJ, 753, 115

Takeuchi T. T., Ishii T. T., Nozawa T., Kozasa T., Hirashita H., 2005, MNRAS, 362, 592

Tanaka H., Inaba S., Nakazawa K., 1996, Icarus, 123, 450

Tazaki R., Tanaka H., Okuzumi S., Kataoka A., Nomura H., 2016, ApJ, 823, 70

Voelk H. J., Jones F. C., Morfill G. E., Roeser S., 1980, A&A, 85, 316

Voshchinnikov N. V., Hirashita H., 2014, MNRAS, 445, 301

Voshchinnikov N. V., Il'in V. B., Henning T., 2005, A&A, 429, 371

Voshchinnikov N. V., Il'in V. B., Henning T., Dubkova D. N., 2006, A&A, 445, 167

Wada K., Tanaka H., Suyama T., Kimura H., Yamamoto T., 2007, ApJ, 661, 320

Wada K., Tanaka H., Suyama T., Kimura H., Yamamoto T., 2008, ApJ, 677, 1296

Wada K., Tanaka H., Okuzumi S., Kobayashi H., Suyama T., Kimura H., Yamamoto T., 2013, A&A, 559, A62

Weingartner J. C., Draine B. T., 2001a, ApJS, 134, 263

Weingartner J. C., Draine B. T., 2001b, ApJ, 548, 296

Williams D. R., Wetherill G. W., 1994, Icarus, 107, 117

Wong Y. H. V., Hirashita H., Li Z.-Y., 2016, PASJ, 68, 67

Woo J. W., Clark G. W., Day C. S. R., Nagase F., Takeshima T., 1994, ApJ, 436, L5

Yamasawa D., Habe A., Kozasa T., Nozawa T., Hirashita H., Umeda H., Nomoto K., 2011, ApJ, 735, 44

Yan H., Lazarian A., Draine B. T., 2004, ApJ, 616, 895

Zubko V. G., Mennella V., Colangeli L., Bussoletti E., 1996, MNRAS, 282, 1321

Zuo W. B., Li A., Zhao G., 2020, ApJS, in press, arXiv:2011.09440

APPENDIX A: DERIVATION OF THE BASIC EQUATIONS

We derive equations (4) and (5) based on O09. We start from the 2D Smoluchowski equation generalized to treat shattering as well as coagulation:

$$\frac{\partial f(\boldsymbol{I}, t)}{\partial t} = -f(\boldsymbol{I}, t) \int K(\boldsymbol{I}; \boldsymbol{I}') f(\boldsymbol{I}', t)\, \mathrm{d}^2 \boldsymbol{I}'$$
$$+ \iint K(\boldsymbol{I}_1; \boldsymbol{I}_2) f(\boldsymbol{I}_1, t) f(\boldsymbol{I}_2, t)\theta(\boldsymbol{I}; \boldsymbol{I}_1, \boldsymbol{I}_2)\, \mathrm{d}^2 \boldsymbol{I}_1\, \mathrm{d}^2 \boldsymbol{I}_2, \qquad \text{(A1)}$$

where f is the distribution function of $\boldsymbol{I} \equiv (m, V)$ (grain mass and volume, respectively) at time t, $K(\boldsymbol{I}_1, \boldsymbol{I}_2)$ is the collisional kernel (product of the collisional cross-section and the relative velocity of the two colliding grains), $\theta(\boldsymbol{I}; \boldsymbol{I}_1, \boldsymbol{I}_2)$ is the distribution function of the produced grains by the collision, and the integration is executed for all the relevant range of $\boldsymbol{I}$, which is usually $[0, \infty] \times [0, \infty]$. We distinguish the two colliding grains with subscripts 1 and 2, referred to as grain 1 and 2, respectively [i.e. $\boldsymbol{I}_1 = (m_1, V_1)$ and $\boldsymbol{I}_2 = (m_2, V_2)$]. The normalization of θ is determined by

$$\int m\theta(\boldsymbol{I}; \boldsymbol{I}_1, \boldsymbol{I}_2)\, \mathrm{d}^2 \boldsymbol{I} = m_1. \qquad \text{(A2)}$$

We note that when we consider the collision of grain 1 with grain 2, we only consider the redistribution of m_1 (i.e. we separately treat the collision of grain 2 with grain 1). This is why only m_1 enters the normalization. Because of this, we do not have a factor of $1/2$ (which appears in O09's expression) before the second term of the right-hand side in equation (A1). The two expressions are mathematically equivalent.

Now we take the zeroth moment of equation (A1) for V, that is, we integrate it for V. We adopt the following form for θ for simplicity and for analytical convenience:

$$\theta(\boldsymbol{I}; \boldsymbol{I}_1, \boldsymbol{I}_2) = \bar{\theta}(m; m_1, m_2)\, \delta[V - V_{1+2}(m; \boldsymbol{I}_1, \boldsymbol{I}_2)], \qquad \text{(A3)}$$

where $\bar{\theta}$ describes the mass distribution function of the grains formed after the collision between grains with $\boldsymbol{I}_1$ and $\boldsymbol{I}_2$, δ is Dirac's delta function, and V_{1+2} describes the volume of the grain formed from the collision between grains 1 and 2 (and the produced grain has a mass of m). This expression assumes that $\bar{\theta}$ is independent of the volume (or porosity) of the original grains and that the volume of the collisional product is determined by $\boldsymbol{I}_1$ and $\boldsymbol{I}_2$ and is a function of m. By integrating both sides of equation (A1) for V, we obtain the equation for the zeroth moment, $\tilde{n}(m, t)$, defined in equation (1). We also take the first moment of equation (A1); that is, we multiply both sides of equation (A1) by V and integrate them for V to obtain the equation for $\bar{V}$ defined by equation (2). The resulting moment equations are written as (see also O09)

$$\frac{\partial \tilde{n}(m, t)}{\partial t} = -\tilde{n}(m, t) \int \bar{K}(m; m_1)\tilde{n}(m_1, t)\, \mathrm{d}m_1$$
$$+ \iint \bar{K}(m_1; m_2)\tilde{n}(m_1, t)\tilde{n}(m_2, t)\bar{\theta}(m; m_1, m_2)\, \mathrm{d}m_1\, \mathrm{d}m_2, \qquad \text{(A4)}$$

$$\frac{\partial \bar{V}(m, t)\tilde{n}(m, t)}{\partial t} = -\tilde{n}(m, t) \int \overline{VK}(m; m_1)\tilde{n}(m_1, t)\, \mathrm{d}m_1$$

$$+ \iint \overline{V_{1+2}K}(m_1; m_2)\tilde{n}(m_1, t)\tilde{n}(m_2, t)\bar{\theta}(m; m_1, m_2)\, \mathrm{d}m_1\, \mathrm{d}m_2,$$

$$(\text{A5})$$

where

$$\bar{K}(m_1; m_2) \equiv \iint K(m_1, V_1; m_2, V_2)\frac{f(m_1, V_1)}{\tilde{n}(m_1)}\frac{f(m_2, V_2)}{\tilde{n}(m_2)}\mathrm{d}V_1\mathrm{d}V_2,$$

$$(\text{A6})$$

$$\overline{VK}(m; m_1) \equiv \iint VK(m, V; m_1, V_1)\frac{f(m, V)}{\tilde{n}(m)}\frac{f(m_1, V_1)}{\tilde{n}(m_1)}\mathrm{d}V\mathrm{d}V_1,$$

$$(\text{A7})$$

$$\overline{V_{1+2}K}(m; m_1, m_2) \equiv \iint V_{1+2}(m; m_1, V_1, m_2, V_2)K(m_1, V_1; m_2, V_2)$$

$$\times \frac{f(m_1, V_1)}{\tilde{n}(m_1)}\frac{f(m_2, V_2)}{\tilde{n}(m_2)}\mathrm{d}V_1\mathrm{d}V_2. \qquad (\text{A8})$$

The integration is performed for $[0, \infty] \times [0, \infty]$. The moment equations, in general, are not closed since a higher-order moment always appears. To close this hierarchy, we adopt the same assumption as O09; that is, the volume is replaced with the mean value at each m. Under this assumption, the distribution function is written as $f(m, V) = \tilde{n}(m)\,\delta[V - \bar{V}(m)]$. O09 refer to this approximation as the volume-averaging approximation, and confirmed that it gives a consistent result with the full solution of the 2D Smoluchowski equation for their coagulation problem. Although there is no guarantee that this approximation is valid for shattering, the increasing filling factor at small grain radii (Section 3.2) is at least qualitatively consistent with the evolution expected from the production of compact fragments by shattering.

Adopting the above volume-averaging approximation, we obtain

$$\bar{K}(m_1; m_2) = K[m_1, \bar{V}(m_1); m_2, \bar{V}(m_2)], \qquad (\text{A9})$$

$$\overline{VK}(m; m_1) = \bar{V}(m)\bar{K}(m; m_1), \qquad (\text{A10})$$

$$\overline{V_{1+2}K}(m; m_1, m_2) = V_{1+2}[m; m_1, \bar{V}(m_1), m_2, \bar{V}(m_2)]\bar{K}(m_1; m_2). \qquad (\text{A11})$$

We apply these relations to equations (A4) and (A5), reorganize the notations as $\bar{K}(m_1; m_2) = K_{m_1, m_2}$, $V_{1+2}[m; m_1, \bar{V}(m_1), m_2, \bar{V}(m_2)] = (V_{1+2})^m_{m_1, m_2}$. and multiply both sides in equation (A4) by m. Finally, introducing $\rho(m, t) \equiv m\tilde{n}(m, t)$ and $\psi(m, t) \equiv \bar{V}(m, t)\tilde{n}(m, t)$, we obtain equations (4) and (5).

This paper has been typeset from a TEX/LATEX file prepared by the author.